Investigating and Predicting spatiotemporal variations in vegetation cover in transitional climate zone: A case study of Gansu (China)

Qing He[1], Kwok Pan Chun[1, 2*], Bastien Dieppois[3], Liang Chen[4], Pingyu Fan[1], Emir Toker[5], Omer Yetemen[5], Xicai Pan[6]

[1] Department of Geography, Hong Kong Baptist University, Hong Kong, China

[2] Department of Geography and Environmental Management, University of the West of England, Bristol, UK

[3] Centre for Agroecology, Water and Resilience (CAWR), Coventry University, Ryton-on-Dunsmore, UK

[4] Key Laboratory of Regional Climate Environment for Temperate East Asia, Institute of Atmospheric Physics, Chinese Academy of Sciences, Beijing, China

[5] Eurasia Institute of Earth Sciences, Istanbul Technical University, Istanbul, Turkey

[6] State Key Laboratory of Soil and Sustainable Agriculture, Institute of Soil Science, Chinese Academy of Sciences, Nanjing, China

***** Corresponding author:

Dr Kwok Pan Chun, kpchun@hkbu.edu.hk; Tel: +852 3411 6541; Fax: +852 3411 5990; Department of Geography, Hong Kong Baptist University, Hong Kong, China.

Abstract

Vegetation ecosystems are sensitive to large-scale climate variability in climate transition zones. As a representative transitional climate zone in Northwest China, Gansu is characterized by a sharp climate and vegetation gradient. In this study, the spatiotemporal variations of vegetation over Gansu are characterized using the satellite-based Normalized Difference Vegetation Index (NDVI) observations during 2000-2020. Results demonstrate that a significant greening trend in vegetation over Gansu is positively linked with large-scale climate factors through modulating the water and energy dynamics. As a climate transition zone, the northern water-limited and southern energy-limited regions of Gansu are affected by water and energy dynamics, differently. In the water-limited region, a weakening Asian monsoon along with colder Central Pacific (CP) and warmer North Pacific (NP) Oceans enhance prevailing westerlies which bring more atmospheric moisture. The enhanced atmospheric moisture and rising temperature promote the local vegetation growth. In contrast, large-scale climate variations suppress the southwest monsoon moisture fluxes and reduce precipitation in southern

energy-limited regions. In these energy-limited regions, temperature has more effects on vegetation growth than precipitation. Therefore, the greenness of vegetation is because of more available energy from higher temperatures despite overall drying conditions in the region. Based on the above mechanism, future scenarios based on both Coupled Model Intercomparison Project Phase 5 (CMIP5) and Coupled Model Intercomparison Project Phase 6 (CMIP6) are developed for vegetation over Gansu. In the near term (2021-2039), the vegetation is likely to increase due to rising temperature. However, the vegetation is expected to decrease in a long term (2080-2099) when the energy-limited regions become water-limited due to increasing regional temperatures and lowering atmospheric moisture flux. This study reveals an increasing desertification risk over Gansu. Similar investigations will be valuable in climate transition regions worldwide to explore how large-scale climate variability affects local ecological services under different future climate scenarios.

Keywords: Vegetation variability; Normalized Difference Vegetation Index (NDVI); climate variability; water dynamic; energy dynamic; Coupled Model Intercomparison Project Phase 5 (CMIP5); Coupled Model Intercomparison Project Phase 6 (CMIP6)

1. Introduction

Vegetation is a natural interface between soil, hydrology, ecosystem and climate, and it is a sensitive indicator of regional environmental change (Cui and Shi 2010). Vegetation variability in different parts of the world varies greatly over the past decades. The vegetation has been increasing in the north of extratropical latitudes (Mao et al. 2016), and South Asia (Wang et al. 2017b), but there are opposite trends in boreal Eurasia (Piao et al. 2011) and Inner Asia (Mohammat et al. 2013). Shifts in vegetation are mainly attributed to global and regional climate changes (Cui and Shi 2010; Li et al. 2015; Xu et al. 2016), land-use changes (Dirnböck et al. 2003; Fernandes et al. 2011; Tasser and Tappeiner 2002), and the carbon dioxide fertilization (Los 2013; Schimel et al. 2000; Yang et al. 2016). Among these factors, climate variability has been recognized as the most direct and important driver for vegetation variations (Cui and Shi 2010; Yang et al. 2019).

Shifting climate patterns play an important role in vegetation spatiotemporal variability, especially in climate transition zones (Xia et al. 2019), including Qinling Mountains in China (Xia et al. 2019) and central Queensland in Australia (Krull et al. 2005). In such climate transition zones, ecosystems are unstable and highly sensitive to regional climate fluctuations (Hou et al. 2019). As a transitional climate zone between humid and arid regions in Northwest China, Gansu is characterized by a sharp climate and vegetation gradient (Wang et al. 2018). Due to global warming, the dry Northwest China has been transformed into a wet region since the last century (Dai et al. 2011), while Northeast China became drier (He et al. 2020). The combinations of wetting and drying trends in the different parts of Gansu make the entire ecosystem more vulnerable. The wetting and drying patterns might be due to shifting regional precipitation and temperature patterns over the region (Dai et al. 2011; Wang et al.

2017a). The regional precipitation and temperature distributions are controlled by large-scale climate variability by modulating regional the water and energy cycles (Ouyang et al. 2014; Xiao et al. 2015). Therefore, detecting changes in vegetation dynamics and identifying their linkages with regional and large-scale climate variability is crucial to regional ecological health assessments and regional economic development coordination under changing climate scenarios.

Over Asian regions, vegetation covers are closely related to the Asian monsoons, i.e. the East Asian monsoon (EAM; Jiang et al. 2006; Zhao and Yu 2012) and the Indian monsoon (IM; Chen et al. 2014; Lee et al. 2009). Vegetation dynamics are also related to sea-surface temperature (SST) modes in the Pacific (Erasmi et al. 2009; Jiang et al. 2011; Lü et al. 2012) and Indian Oceans (Li et al. 2017). For example, climatological anomalies in vegetation cover over Indonesia were associated with increases in extreme events (especially droughts) in response to El Nino Southern Oscillation (ENSO; Erasmi et al. 2009). Similarly, ENSO was demonstrated to affect the vegetation cover in China (Jiang et al. 2011; Lü et al. 2012).

All previous studies suggested that Asian monsoons and SST oscillations affect regional or local vegetation growths through the modulation of local climate variables. However, the relationships between vegetation and local climate variables including precipitation, evaporation and temperature are not consistent in previous studies (Li et al. 2009; Xu et al. 2016; Zhao et al. 2011). When Li et al. (2009) found that precipitation and temperature are both significantly related to vegetation, Zhao et al. (2011) suggested that the role of temperature is insignificant. Moreover, Xu et al. (2016) found that grassland and cropland have different responses to precipitation, evaporation and temperature. In this study, we establish hydroclimate mechanisms over Gansu based on both water and energy dynamics to link the large-scale climate variability with local vegetation. Based on this mechanism, we will produce the future projections of vegetation based on climate model outputs for 2021-2039 and 2080-2099. Overall, this study aims to: i) investigate the spatiotemporal changes in vegetation over Gansu; ii) establish water and energy mechanisms between climate drivers and vegetation variation; and iii) develop future scenarios for spatiotemporal changes in vegetation based on climate models outputs.

The paper is structured as follows. In Sections 2 and 3, we introduce the materials and methods. In Section 4, the spatiotemporal vegetation variations and its linkages with local and large-scale climate variability over Gansu are investigated. In the final section, the implications and possible future applications related to desertification risks are summarized and discussed for climate transition zones.

2. Materials

2.1 Study area

In the inner land of Northwest China, Gansu has plateau terrain inclined from South-west to North-east, with an elevation from 598 to 5602 m above the sea level (a.s.l.) (An et al. 2019). It lies between 93°E-110°E and 32°-44°N, with a total area of 455,000 km^2 (Figure 1). Based on Zhao (1983), Gansu can be divided into three natural geographical regions by 3000 m a.s.l. elevation contour and 400 mm contour of annual precipitation (Figure 1): the Hexi Corridor arid region (HCAR), the Qinghai-Tibet alpine region (QTAR), and the Loess Plateau semi-arid region (LPSR). The Gansu region straddles the alpine, semi-arid and arid climatic zones, which make it vulnerable to climate change (Li et al. 2013). The annual average temperature is around 0-14°C, and it varies greatly from the cold QTAR (western part) to the warm HCAR and LPSR (eastern part) (Wang et al. 2014b). Annual average precipitation varies from 50 mm.yr^{-1} in the northwest to 500 mm.yr^{-1} in the southeast region (Cheng and Falkenheim 2016). Over the Gansu region, precipitation concentrates between June and September during the Asia summer monsoon season, and it shows strong interannual variations (Li et al. 2013). The main land and vegetation types are deserts, grassland and forest (Wang et al. 2014b). It has been suggested that intensive climate variations have placed a heavy pressure on the local fragile ecological and hydroclimate systems and they have impeded the sustainable agricultural and economic development in the region (Han et al. 2015; Wang et al. 2003).

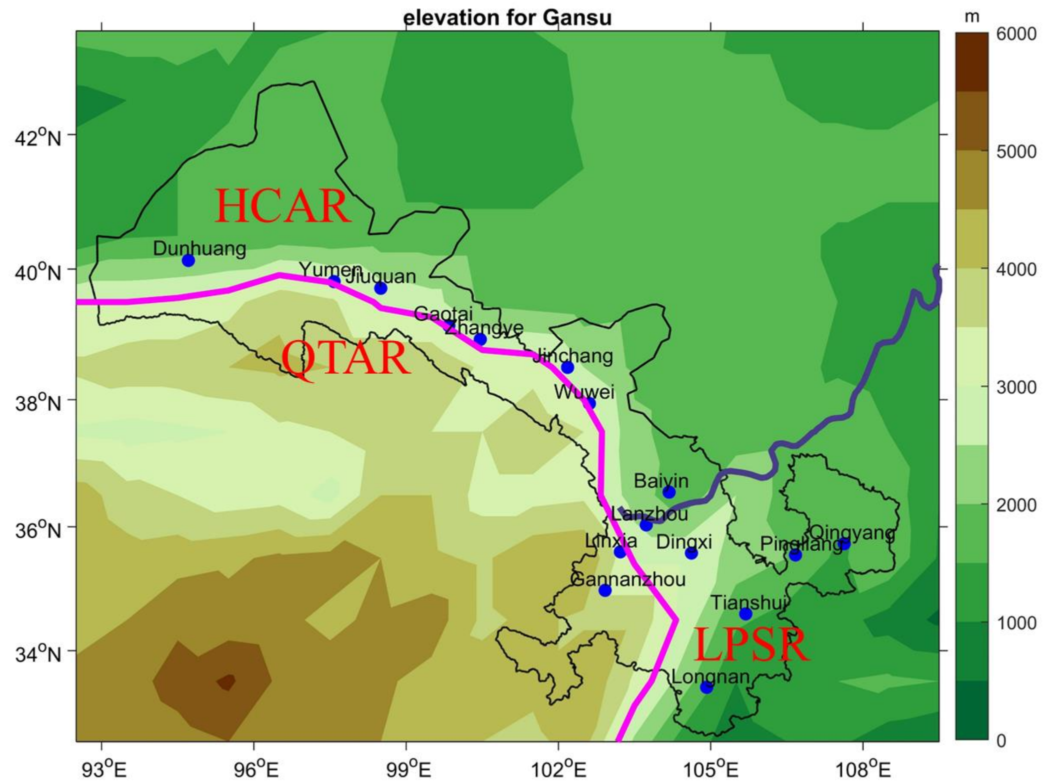

Figure 1. The elevation with 16 locations (blue dots) over Gansu. The magenta (elevation contour at 3000 m a.s.l.) and purple line (annual precipitation contour at 400 mm) divide the Gansu into three graphically regions: the Hexi Corridor arid region (HCAR), the Qinghai-Tibet alpine region (QTAR), the Loess Plateau semi-arid region (LPSR).

2.2 Data

Vegetation indicators are extracted from satellite products, and meteorological variables and climate indices are derived from reanalysis datasets. The details of the datasets are summarized in Table 1.

Table 1. The information of datasets used in this study.

Datasets	Variables	Spatial extent, resolution	Temporal extent, resolution	Reference
MOD12C2	NDVI	Global, 0.05×0.05°	2000/02-present, monthly	Didan (2015)
ERA5-Land	Precipitation, actual evapotranspiration (AET), temperature, potential evapotranspiration (PET)	Global, 0.1×0.1°	1981/01-present, monthly	Muñoz (2019)
ERA5	Wind, specific humidity, CAPE	Global, 0.25×0.25°	1979/01-present, monthly	Hersbach et al. (2019)
ERSST.v5	SST	Global, 2×2°	1984/01-present, monthly	Huang et al. (2017)

2.2.1 Normalized Difference Vegetation Index (NDVI)

Vegetation cover is widely and continuously monitored by satellite remote sensing (Yang et al. 2019). The Normalized Difference Vegetation Index (NDVI) is one of the most widely used remote sensing measures, and many NDVI products have continuous records over decades (e.g., Li et al. 2010b; Mkhabela et al. 2011; Zhang et al. 2003). Here, the NDVI dataset is derived from the Terra Moderate Resolution Imaging Spectroradiometer (MODIS) product MOD13C2 in a spatial resolution of 0.05×0.05° at a monthly time-step (Didan 2015). The NDVI dataset is extracted from the National Aeronautics and Space Administration (NASA) Land Processes Distributed Active Archive Center (LP DAAC; https://e4ftl01.cr.usgs.gov/MOLT/MOD13C2.006/). The MODIS NDVI has been widely applied in large-scale vegetation studies (e.g., Badreldin et al. 2014; Li et al. 2015; Xu et al. 2016). In this study, the NDVI is used to explore the spatiotemporal variability in vegetation cover between February 2000 and January 2020 (total of 20 years), a period that has not been largely explored in previous studies.

2.2.2 Moisture budgets

The vegetation growths are mainly controlled by water and energy balances. To investigate regional changes in vegetation and their link to water and energy variability, we examine moisture dynamics that associate with water and energy cycles (Peng and Zhou 2017). The atmospheric moisture conservation equation in flux form of vertical integration is written as (Trenberth et al. 2011):

$$\frac{\partial W}{\partial t} = AET - P - \nabla \cdot Q \qquad (1)$$

where W is the total column water vapor, AET is the actual evapotranspiration, P is the precipitation, and $\nabla \cdot Q$ represents the vertically-integrated atmospheric moisture flux divergence (hereafter called MFD). The tendency term $\frac{\partial W}{\partial t}$ is small for long-term means. The equation (1) can be written as

$$P + \nabla \cdot Q \approx AET \qquad (2)$$

The primary balance of moisture is thus between $P + \nabla \cdot Q$ (gaining moisture) and AET (losing moisture). For a region, water mainly comes from precipitation brought by horizontal moisture movements and vertically convective activities. To represent the horizontal water movement, vertically integrated moisture fluxes and MFD are used. AET is a key factor in the water cycle, but also an important part in the energy cycle in the form of latent heat (Trenberth et al. 2011). To study thermally vertical motion, the Convective Available Potential Energy (CAPE), a measure of energy available for lifting air parcels from the lower to the upper atmosphere, is used. Therefore, both horizontal and vertical dynamics are used to examine the effects of water and energy on vegetation. From the above framework, AET acts as a bridge or fluxes between the water and energy cycles.

The precipitation, AET and temperature data are obtained from the ERA5-Land monthly averaged datasets between 1981 and 2020 (https://cds.climate.copernicus.eu/cdsapp#!/dataset/reanalysis-era5-land-monthly-means?tab=form) (Muñoz 2019). By including improved land surface processes, the ERA5-Land reanalysis datasets provide higher spatial resolution data (0.1°×0.1°) than its driven climate reanalysis data (0.25°×0.25°) (Muñoz 2019). Many studies recommended the use of Tropical Rainfall Measuring Mission (TRMM) data to estimate precipitation over China (e.g., Cao et al. 2018; Ferreira et al. 2013; He et al. 2020). In Figure A1, ERA5-Land and TRMM precipitation data are very comparable, with high-correlation levels and high significances. It suggests the reliability of ERA5-Land datasets over Gansu. MFD and CAPE, which are not available in ERA5-Land, are extracted from ERA5 data over the same period, but with a spatial resolution of 0.25°×0.25° (https://cds.climate.copernicus.eu/cdsapp#!/dataset/reanalysis-era5-pressure-levels-monthly-means?tab=form) (Hersbach et al. 2019).

2.2.3 Water-limited and energy-limited environments

Vegetation growths are affected by both water and energy factors. In this study, to determine the dominating factors, we employ the concept of water-limited and energy-limited environments

(Parsons and Abrahams, 1994). Based on the Parsons and Abrahams (1994), a water-limited (energy-limited) environment is defined as the areas having a P.PET^{-1} (potential evapotranspiration) ratio lower (greater) than 0.75. The PET data is also derived from the ERA5-Land dataset. The majority of the QTAR area is energy-limited because the P and PET ratio is higher than 0.75, while the HCAR is water-limited with the P and PET ratio lower than 0.75, and the LPSR is a mixed energy- and water-limited region (Figure 2). Therefore, vegetation growth in the HCAR is limited by the availability of precipitation but not temperature (Javadian et al. 2020; Parsons and Abrahams 1994); whereas, in the energy-limited QTAR and some parts of LPSR, the growth of vegetation is mainly restricted by the temperature (Gokmen et al. 2013; Parsons and Abrahams 1994).

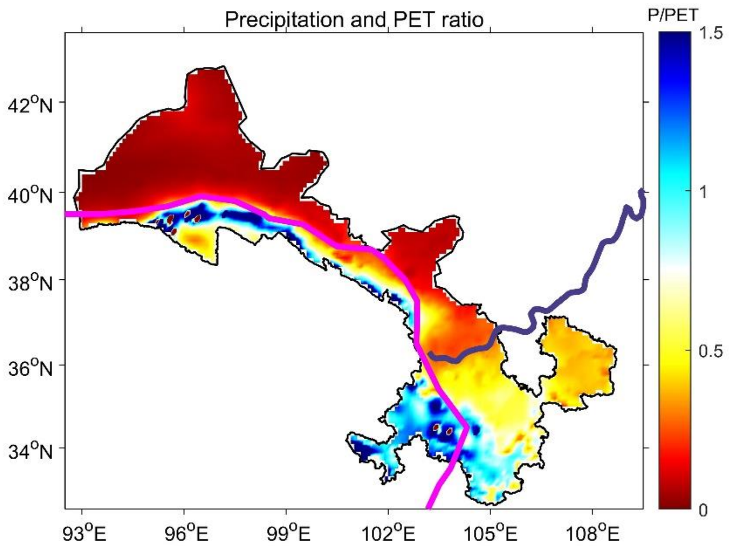

Figure 2. The distribution of the ratio of precipitation and PET. Warm colour denotes the water-limited regions (i.e., a ratio less than 0.75), while cool colour indicates the energy-limited regions (i.e., ratio larger than 0.75). The magenta and purple lines divide the Gansu into three graphically regions (c.f. Figure 1).

2.2.4 Large-scale climate variability

As suggested by previous studies, precipitation and vegetation variability over Asia are controlled by Asian monsoons (Chen et al. 2014; Jiang et al. 2017; Lee et al. 2009; Zhao and Yu 2012), the tropical Pacific Ocean temperatures (Erasmi et al. 2009; Jiang et al. 2011; Lü et al. 2012), the North Pacific SST (Ao and Sun 2016; Li and Li 2000; Zhou and Xia 2012), and the Indian SST variability (Li et al. 2017; Tong et al. 2019). These large-scale ocean oscillations are estimated through SST indices using the Extended Reconstructed SST version 5 (ERSSTv.5; https://www.ncdc.noaa.gov/data-access/marineocean-data/extended-reconstructed-sea-surface-temperature-ersst-v5) (Huang et al. 2017). Derived from the International Comprehensive Ocean-Atmosphere Dataset (ICOADS) Release 3.0., the ERSST.v5 spans between 1854 and 2020 at a 2°× 2° grid resolution. Compared to its previous versions, the ERSST.v5 uses the Empirical Orthogonal Teleconnections (EOTs) to reduce high-latitude damping, which improves the SST spatial and temporal variability of the product (Huang et al. 2017).

Among different kinds of Asian monsoons, and the SST indices in the Pacific and Indian Oceans, the Webster and Yang Monsoon (WYM), the Central Pacific El Nino oscillation (CP) and the North Pacific SST anomalies (NP) are found to be the more significant contributors to NDVI-based vegetation variability to Gansu (Figures A2-A3). The WYM is computed using the difference between zonal winds at 850-hPa and 200-hPa over the Indian region (0-20°N, 40°-110°E; Webster and Yang 1992). The SST indices for the CP and the NP are respectively calculated according to the definitions provided in Kao ad Yu (2009) and Mantua (1997). The CP pattern is different from the eastern type of ENSO (EP; the traditionally defined ENSO type), and these Pacific SST patterns affect precipitation over China differently (Lv et al. 2019). The western North Pacific subtropical high (WNPSH) was suggested to be more strongly related to the CP than to the EP (Weng et al. 2011). The WNPSH plays significant role in regulating the hydroclimate system in China (Gao et al. 2020). Therefore, the CP is expected to be responsible for vegetation changes through its effects on local climate systems over China. In addition, the NP has been shown to contribute to precipitation variability over China (Ao and Sun 2016; Li and Li 2000; Zhou and Xia 2012), and it thus might affect vegetation growth in the transition regions of China.

2.2.5 Climate Change Scenarios

The Coupled Model Intercomparison Project Phase 5 (CMIP5) and Phase 6 (CMIP6) model outputs have been widely used for evaluating future conditions of vegetation (Zhao et al. 2020; Zhou et al. 2020). Compared to previous phases, CMIP5 models include more carbon processes and feedback mechanisms of climate systems while CMIP6 have finer resolution with improved dynamical processes (Eyring et al. 2016; Taylor et al. 2012). In this study, the SST and wind fields from CMIP5 models (Table2) and CMIP6 models (Table 3) are used to derive the atmosphere-ocean oscillation indices. The CMIP5 models are based on the historical scenarios between 1850 and 2005 and three future scenarios (RCP 2.6, RCP 4.5 and RCP 8.5) between 2006 and 2100. The RCP 2.6 corresponds to a strongly declining emission scenario, leading to warming of well below 2°C, which is compatible with the Paris Agreement. The RCP 4.5 scenario corresponds to an approximate doubling (medium emission scenario) in carbon dioxide relative to the pre-industrial level, whereas the RCP 8.5 scenario represents a more than threefold increase (high emission scenario) (Swain and Hayhoe 2015). It is worth noting that the SST and wind fields data under RCP 2.6 are unavailable for most CIMP5 models in Table 2. Therefore, only four models are used for RCP 2.6, including bcc-csm1-1-m, IPSL-CM6A-MR, MPI-ESM-LR and NorESM1-M. For CMIP6, similarly, atmosphere-ocean oscillation indices were estimated based on the historical scenarios (1850-2014) and two Shared Socioeconomic

Pathways (SSP), including SSP1-2.6, SSP2-4.5 and SSP5-8.5. For four CMIP6 models, total 51 simulations were used: 10 members (r1i1p1f1 to r1i10p1f1) for ACCESS, 25 members (r1i1p1f1 to r1i25p1f1) for CanESM5, 6 members for IPSL (i.e., r1i1p1f1, r1i2p1f1, r1i3p1f1, r1i4p1f1, r1i6p1f1 and r1i14p1f1), and 10 members for MIROC (r1i1p1f2 to r1i10p1f2). In this study, two future periods are used for investigating the transitional changes of vegetation between 2021 and 2099: 2021-2039 (2030s) and 2080-2099 (2090s).

Table 2. Details of 13 CMIP5 climate models used in this study.

Model	Institution	Lon×Lat
ACCESS1-0	Commonwealth Scientific and Industrial Research Organization (CSIRO) and Bureau of Meteorology (BOM), Australia	1.875×1.25°
ACCESS1-3	Commonwealth Scientific and Industrial Research Organization (CSIRO) and Bureau of Meteorology (BOM), Australia	1.875×1.25°
CESM1-BGC	National Center for Atmospheric Research, USA	1.25×0.9375°
CNRM-CM5	Centre National de Recherches Météorologiques/Centre Européen de Recherche et For-mation Avanc´ees en Calcul Scientifique, France	~1.4×1.4°
GFDL-CM3	Geophysical Fluid Dynamics Laboratory (GFDL), New Jersey	2×2.5°
GFDL-ESM2M	Geophysical Fluid Dynamics Laboratory (GFDL), New Jersey	2×2.5°
HadGEM2-CC	Met Office Hadley Centre, UK	1.875×1.25°
IPSL-CM5A-LR	Institut Pierre-Simon Laplace (IPSL), France	3.75×1.875°
MPI-ESM-LR	Max Planck Institute (MPI) for Meteorology, Germany	1.875×1.875°
NorESM1-M	Bjerknes Centre for Climate Research, Norwegian Meteorological Institute, Norway	2.5×1.875°
NorESM1-ME	Bjerknes Centre for Climate Research, Norwegian Meteorological Institute, Norway	2.5×1.875°
bcc-csm1-1	Beijing Climate Center (bcc), China Meteorological Administration, China	~2.8×2.8°

inmcm4	Russian Academy of Sciences, Institute of Numerical Mathematics, Russia	2×1.5°

Table 3. Details of 4 CMIP6 climate models used in this study.

CMIP6	Institution	Lon×Lat
ACCESS-ESM1-5	Commonwealth Scientific and Industrial Research Organization (CSIRO)-Australia Research Council Centre of Excellence for Climate System Science (ARCCSS), Australia	1.25×1.875°
CanESM5	Canadian Centre for Climate Modelling and Analysis, Canada	2.8×2.8°
IPSL-CM6A-LR	Institute Pierre-Simon Laplace (IPSL), France	1.26×2.5°
MIROC-ES2L	The University of Tokyo, National Institute for Environmental Studies, and Japan Agency for Marine-Earth Science and Technology, Japan	1.4×1°

3. Methods

3.1 Mann-Kendall Test

The Mann-Kendall (MK) test is a nonparametric method to quantify the significance of linear temporal trends (Kendall 1975; Mann 1945). Previous work argued that the results of the MK trend test could be misleading if serial correlations and outliers are ignored (Hamed 2008; Hamed and Ramachandra Rao 1998; Khaliq et al. 2009). In this study, the MK test is modified, according to Hamed and Ramachandra Rao (1998), to examine the trend significance of NDVI and climate variability. Trend intensity is estimated based on Thiel-Sen's slope, which is robust to outliers (Sen 1968).

3.2 Generalised least square (GLS) regression

Vegetation covers over Gansu are hypothesized to be related to monsoons and SST anomalies in Pacific Oceans. The Generalised least square (GLS) regression models for NDVI values with the adjustments of serial correlations are expressed as:

$$NDVI_m = \beta_0 + \beta_{WYM}WYM + \beta_{CP}CP + \beta_{NP}NP \quad (3)$$

where $NDVI_m$ is the modelled NDVI, and β_{WYM}, β_{CP}, and β_{NP} are the regression coefficients for their corresponding monsoon and SST indices for the Central and North Pacific Oceans. The GLS model is only based on large-scale processes, as CMIP5 models are more likely to perform better to reproduce these processes than local precipitation and temperature (Wang et al. 2014a). In this study, for future vegetation projection, near-term (2030s: 2021-2039) and long term (2090s: 2080-2099) will be used.

3.3 Bias correction

Before developing the empirical regression models, bias-corrections have been applied to winds and SST model outputs, to reduce differences between climate model outputs and reference data sets (ERA5 and ERSSTv.5). Based on cumulative distribution function (CDF), a quantile mapping method by Panofsky and Brier (1958) is used to reduce biases due to scale gaps between the numerical model grid and the scale of investigated processes. This quantile mapping method has been widely applied in hydrological impact studies (Boé et al. 2007; Li et al. 2010a; Shukla et al. 2019) and regional climate change investigations (Fowler et al. 2007; Grillakis et al. 2013; Miao et al. 2016). For a variable x, the method can be expressed as:

$$x_{BC} = F_r^{-1}\left(F_m(x_m)\right) \quad (4)$$

where F_r^{-1} is the inverse CDF of the reference data set, *i.e.* ERA5 and ERSSTv.5, and F_m is the CDF of modelled climate indices from CMIP5 and CMIP6. x_m are the modelled variables and x_{BC} are the bias-corrected outputs.

3.4 Evaluation of GLS model skills and Bias-correction performances

To evaluate the performance of the GLS models for the NDVI estimation and the bias-correction procedures, the leave-one-out cross-validation method (LOOCV) is used. For each validation, *n* samples are randomly divided into a training set with *n-1* samples and a test set with one sample. All the cross-validations are done based on 200-simulation ensembles. The cross-validation error (CVE) is defined as:

$$CVE = \frac{1}{p}\sum_{i=1}^{p}\left(f\left(X(test)\right) - Y(test)\right)^2 \quad (5)$$

where $f(\cdot)$ is the GLS model and bias-correction procedure developed from the training sets using equation (3) or (4). $X(test)$ and $Y(test)$ are the corresponding test sets. The value is closer to 0, and the performances of the GLS model and the bias-correction procedures are better.

We then further examine the GLS model performance in simulating the historical NDVI variability using the mean square error (MSE) and the ratio of standard deviation (RSD). The MSE, one of the most common estimates of errors, is written as:

$$MSE = \frac{1}{n}\sum_{i=1}^{n}(x_i - x_r)^2 \quad (6)$$

where x_r is the reference climate index of x_i.

The RSD is defined as:

$$RSD = \frac{\sigma_m}{\sigma_r} \quad (7)$$

where σ_m and σ_r are the standard deviations of modelled and referenced datasets.

4. Results

4.1 Vegetation patterns

Over the Gansu region, the mean annual NDVI shows a North-South gradient, with more vegetation in the North than in the South (Figure 3a). In different geographical areas of Gansu, the averaged NDVI value of the LPSR is the highest (0.2 ≤ NDVI ≤ 0.7), whereas the averaged NDVI value of QTAR (0 ≤ NDVI ≤ 0.5) is higher than that of the HCAR (0 ≤ NDVI ≤ 0.2; Figure 3a). All three regions show significant increasing trends in the NDVI (Figure 3b). The increasing trend in the NDVI is however more pronounced in regions with greater mean vegetation cover (Figure 3a-b): the LPSR area has the highest increasing NDVI trend, while HCAR has the lowest.

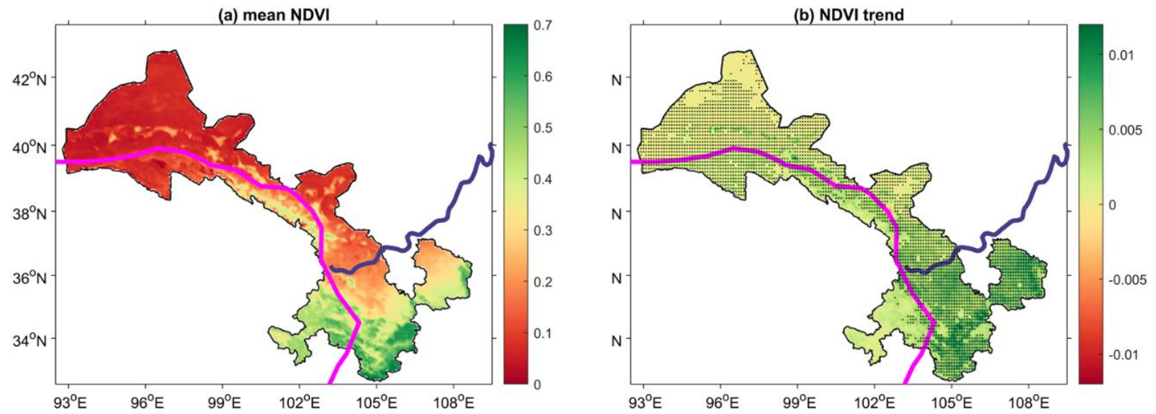

Figure 3. The mean NDVI (a) and NDVI trend (b) between February 2000 and 2020 January. Black dots indicate the trends are statistically significant at p<0.1 according to the MK trend test. The magenta and purple lines divide the Gansu into three graphically regions (c.f. Figure 1).

4.2 Local water and energy patterns and vegetation covers

The spatiotemporal patterns of vegetation growth are related to the variations of local water-energy dynamics. The local water-energy dynamics are usually represented by variations in local precipitation, AET and temperature. In Figure 4a, the average annual precipitation amount shows a similar spatial pattern to the averaged NDVI (Figure 3a): The LPSR and the QTAR receive more than 480 mm.yr^{-1}, but most of the HCAR receive less than 200 mm.yr^{-1}. It suggests that vegetation is denser where precipitation is relatively higher. It is also noted that a decreasing trend in precipitation over the southern regions and an increasing trend in northern regions between 2000 and 2020 (Figure 4b). Regarding AET, mean spatial patterns and trends are consistent with precipitation (Figure 4a-d): i) AET is very low in the HCAR, as there is little water for local evaporation; ii) higher AET is found in the LPSR and the QTAR. Consistently with precipitation trend patterns, AET is thus decreasing in southern regions, but increasing in northern areas (Figure 4d). Therefore, in terms of water dynamics, AET appears to balance the long-term changes in precipitations. In the southern (northern) region with less (more) precipitation, the AET is less (more). Over the QTAR, the average temperature is below 0°C, while the LPSR and the HCAR have a temperature ranging from 5 to 15°C (Figure 4e). As shown in previous global study results (Turkington et al. 2019), most of the Gansu region experiences warming (Figure 4f). Figure 5 shows the regression maps of how the vegetation is related to local water and energy variations. The precipitation, AET and temperature show significant positive relationships with vegetation covers (Figure 5). Precipitation and temperature provide the water and energy to sustain the vegetation growth. More AET suggests more latent heat flux and water vapor in the atmosphere, helping the formation of precipitation (Yang et al. 2018). Therefore, AET favours vegetation growth by both providing more energy and promoting the local water cycle.

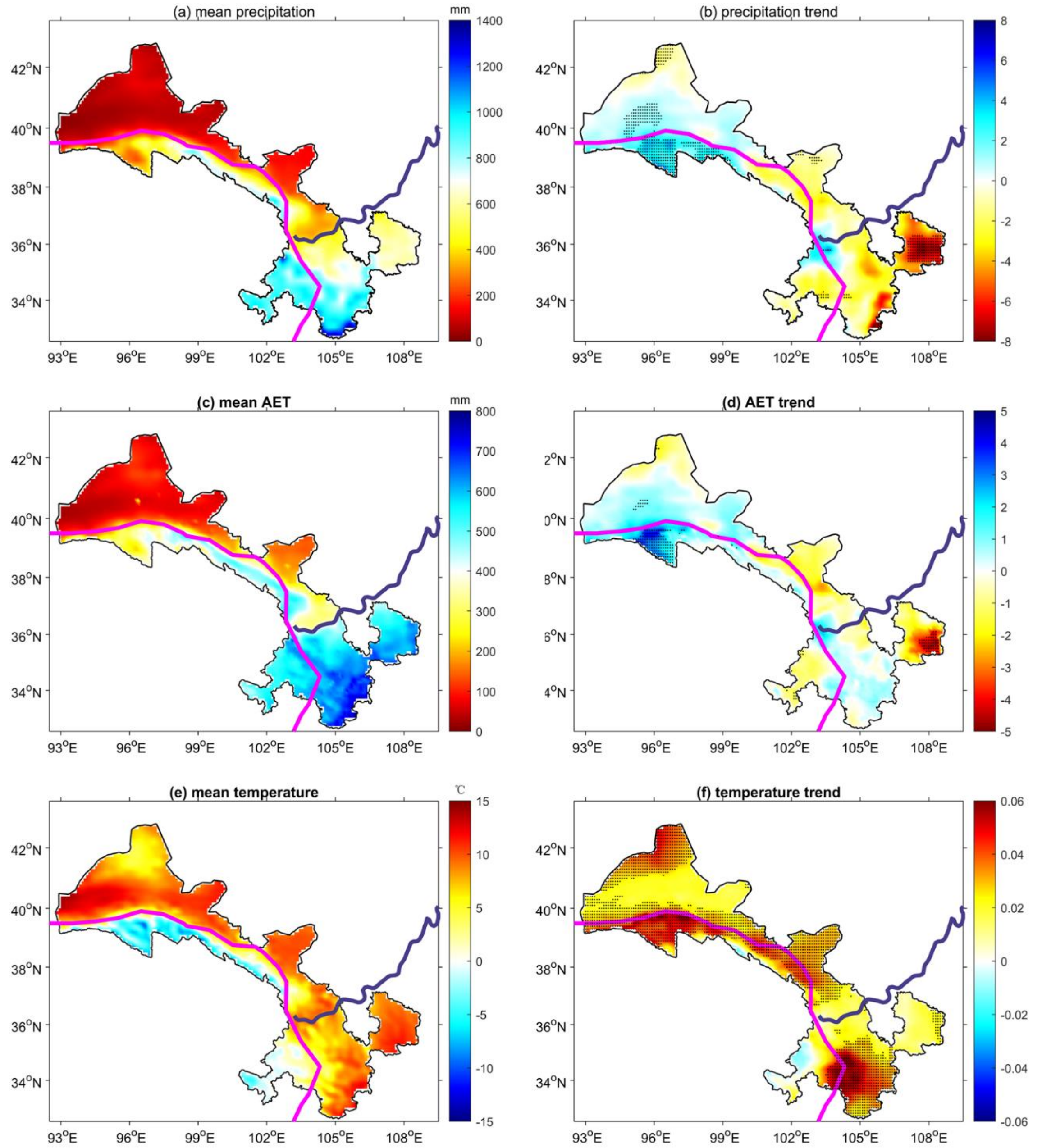

Figure 4. The mean and trend of precipitation (a-b), AET (c-d) and temperature (e-f) between February 2000 and January 2020 over Gansu. Black dots indicate the trends are statistically significant at p<0.1 according to the MK trend test. The magenta and purple lines divide the Gansu into three graphically regions (c.f. Figure 1).

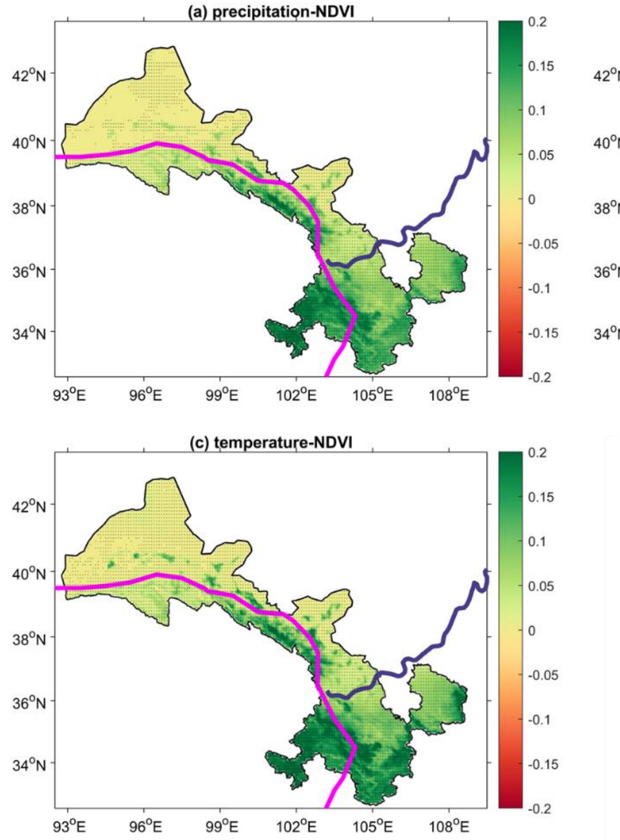

Figure 5. The NDVI regressed map with precipitation (a), AET (b) and temperature (c) between February 2000 and 2020 January. Black dots indicate significant values at the 0.1 significance level according to the t-test. The magenta and purple lines divide the Gansu into three graphically regions (c.f. Figure 1).

4.3 Large-scale atmosphere-ocean variability and vegetation covers

Large-scale atmosphere-ocean variability modulates regional energy and water circulations which affect local vegetation variations. In Section 4.2, the precipitation, AET and temperature show significant positive relationships with vegetation covers. Figure 6 shows the impacts of monsoon (i.e., WYM) and Pacific SST variability (i.e., CP and NP) on regional water, energy and vegetation. The WYM and CP indices show significantly positive relationships with precipitation, AET and temperature (Figure 6a-b, d-e, g-h). According to the positive relationships between vegetation and precipitation, AET and temperature (Figure 5), it is suggested that the WYM and CP could promote local vegetation growth by providing more water and energy (i.e., more precipitation and AET, and higher temperature). The positive contributions of WYM and CP to vegetation are also validated in Figure 6j-k. As opposed to WYM and CP, NP mainly shows negative, but non-significant, relationships with precipitation, AET and temperature over Gansu (Figure 6c, f, i). Interestingly, the NP is significantly and positively related to vegetation (Figure 6l), but it has non-significant relationships (even at $p<0.1$) with regional water and energy variables over most regions (Figure 6c, f, i). Therefore, the accumulated weak energy and water effects of NP appear to have significant impacts on vegetation growth.

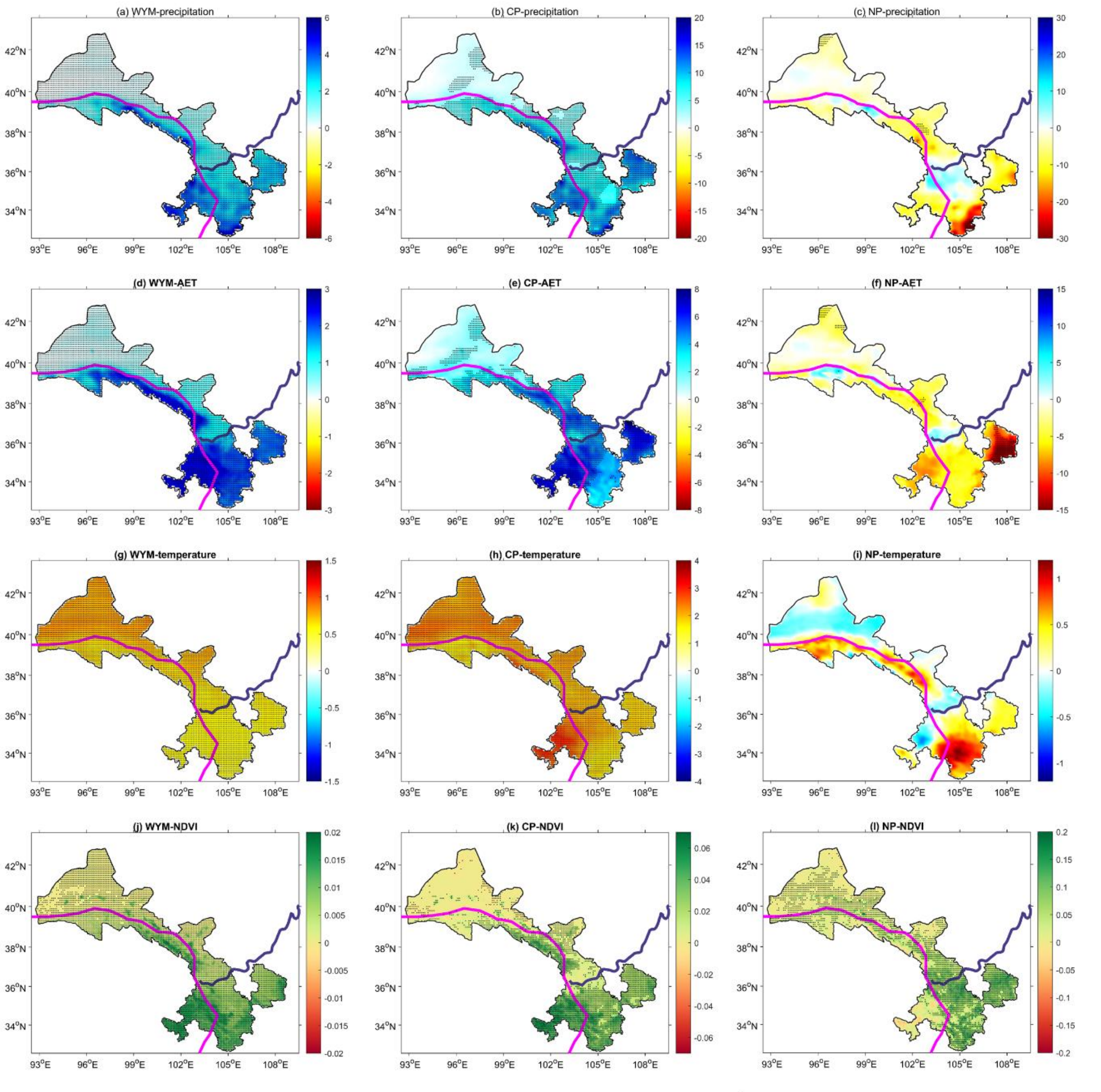

Figure 6. The precipitation (a-c), AET (d-f), temperature (g-i) and NDVI (j-l) regressed map with WYM, CP and NP between February 2000 and 2020 January. Black dots indicate significant values at the 0.1 significance level according to the t-test. The magenta and purple lines divide the Gansu into three graphically regions (c.f. Figure 1).

To investigate the mechanisms driving these positive relationships between vegetation variations and large-scale climate variability, horizontal (i.e., MFD) and vertical water and energy dynamics (i.e., CAPE) are examined in Figures 7 and 8.

Figure 7 shows how the monsoon and the Pacific SST oscillations are related to vertically integrated horizontal moisture movement. Over Gansu, climatological moisture patterns are controlled by prevailing westerly and Asian monsoons (Figure 7a; Ren et al. 2016). Prevailing westerly brings moisture from Euro-Atlantic regions to the north part of Gansu, while the south-westerly moisture fluxes from the Indian Ocean and the south-easterly fluxes from the Pacific bring the atmospheric moisture to South Gansu (Figure 7a). Westerly winds and monsoon moisture fluxes generally converge in the Gansu midlands (Figure 7a). Both WYM and CP are mainly positively related to south-westerly moisture fluxes to China, even though the CP pattern would be weaker (Figure 7b-c). On the contrary, WYM and CP both suppress the westerly moisture fluxes from the Euro-Atlantic regions (Figure 7a-c). Different from WYM and CP, NP is negatively related to south-westerly moisture fluxes but positively related to south-easterly fluxes (Figure 7d). This suggests that a warm North Pacific would lead to less moisture from the Indian Ocean but more water vapour from the Pacific Ocean to China. Such opposite impacts of NP on the different moisture fluxes contributing to the Gansu water balance may explain its weak impacts on local water and energy variables (Figure 6c, f, i). Different circulation effects may interact with each other, thus masking the NP impacts on local climate variables.

In Figure 8b-d, WYM and CP have significantly positive relationships with CAPE, but NP suppresses CAPE over Gansu. Generally, CAPE is very small over Gansu (smaller than 200 J kg^{-1}) in Figure 8a. Low CAPE suggests that the atmosphere is not convective in the region. Moreover, there is no trend in CAPE during 2000 and 2020 (Figure A4). Therefore, the weak CAPE in the region has a limited role in local thermodynamic effects on vegetation although large-scale climate variability has impacts on the CAPE strength.

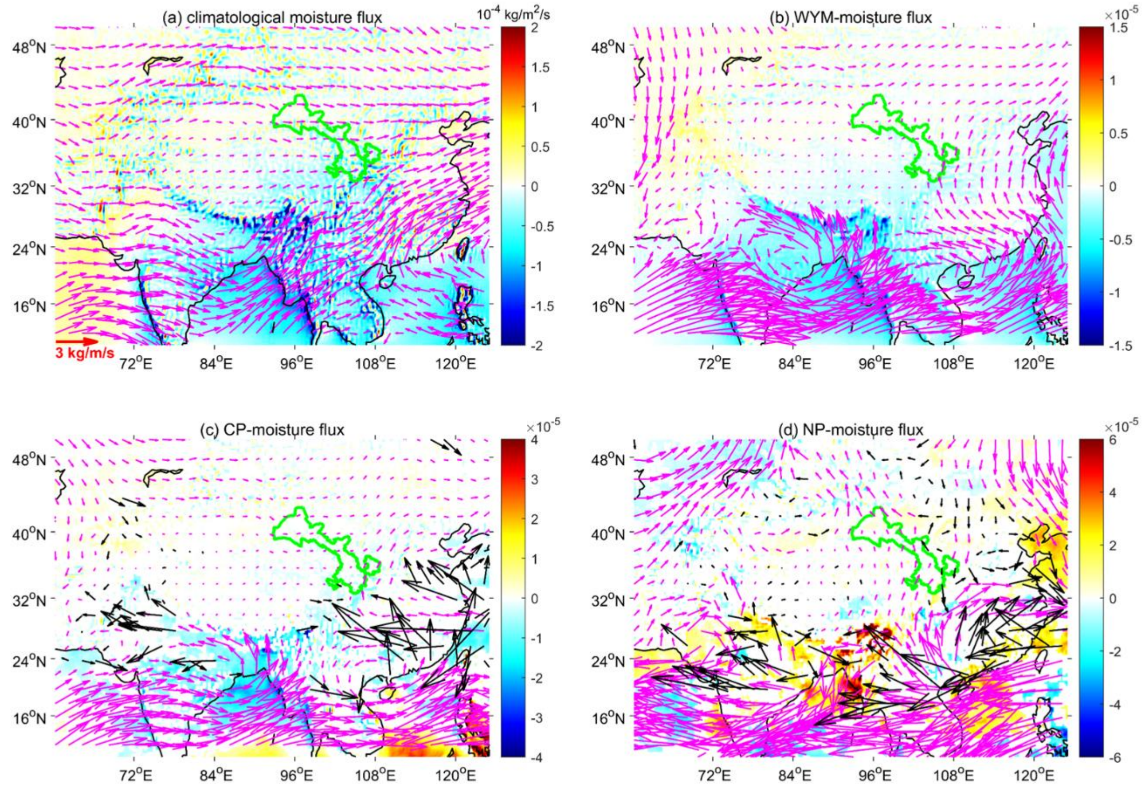

Figure 7. The mean state of the vertical integral of water vapour flux (a), and the regression with the WYM (b), the CP (c) and the NP (d) during betweenFebruary 2000 and January 2020. The magenta arrows in (a) are averaged moisture fluxes and shadings are moisture flux divergence. The magenta and black arrows in (b-c) are significant (*p*<0.1) and non-significant results at *p*>0.1, respectively. For the shaded area, only significant values are presented at the 0.1 significance level according to the t-test.

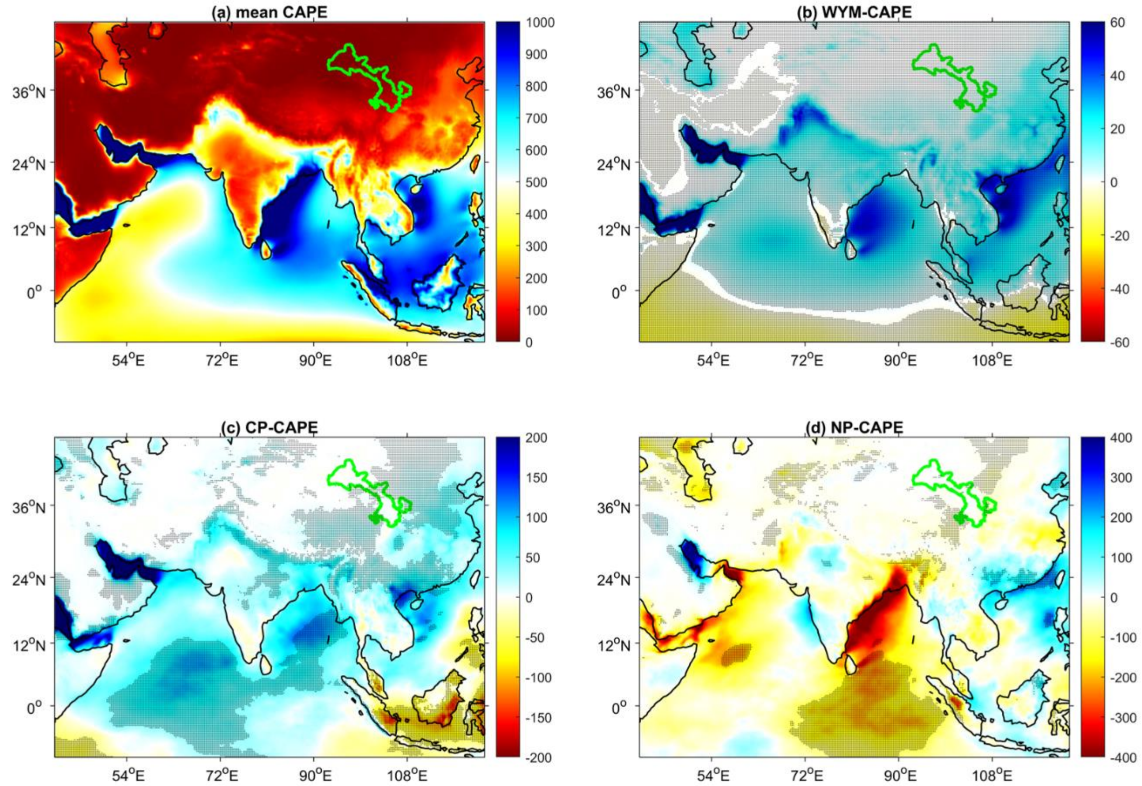

Figure 8. The mean state of CAPE (a), and the regression with the WYM (b), the CP (c) and the NP (d) during February 2000 and January 2020. Black dots indicate significant values at the 0.1 significance level according to the t-test.

4.4 Impact scenarios for vegetation cover in Gansu

After investigating how WYM, CP and NP are related to vegetation variations over the Gansu region, CMIP5 and CMIP6 outputs are used to explore how vegetation cover is likely to change over the 21st century over the Gansu region under different emission scenarios.

4.4.1 Bias-correction and cross-validation

WYM, CP and NP indices are computed for CMIP5 and CMIP6 models, and are bias-corrected, before developing future scenarios for vegetation covers using the GLS regression models. Figure 9 shows the bias-corrected CDF results of historical simulations from CMIP5 (Figure 9a-c) and CMIP6 (Figure 9d-f) against the original CDFs from the reference datasets. The WYM index derived from the CMIP5 outputs overestimates the minimums of WYM values (between -20 and -5) and underestimates the maxima of monsoon values (between -5 and 20; Figure 9a). The CP index derived from the CMIP5 model overestimates CP-Nina conditions and underestimates CP-Nino conditions (Figure 9b). The modelled NP values from the CMIP5 outputs are all underestimated (Figure 9c). The WYM, CP and NP indices from CMIP6 outputs show similar results to CMIP5 (Figure 9d-f). Specifically, the CP index from CMIP6 matches better with referenced data compared to that from

CMIP5 (Figure 9b, e). After the bias corrections, the CDFs of the climate indices derived from CMIP5 and CMIP6 match well with their reference distributions (Figure 9). Between simulated and referenced climate indices, the MSEs of the WYM, the CP and the NP are reduced by 41% and 40%, 95% (76%) and 96% (97%) for CMIP5 (CMIP6) outputs, respectively. For the cross-validation results of bias-correction procedures, the CVE values are 0.537 and 0.385 for WYM, 0.045 and 0.052 for CP and 0.004 and 0.003 for NP from CMIP5 and CMIP6, respectively, and they are in the same magnitude as the MSE. Before projecting NDVI, the GLS model is also cross-validated (Figure 10). The CVE values of the NDVI over Gansu are lower than 0.01, which is in the order magnitude of the MODIS NDVI accuracy, suggesting that the GLS regression model performs adequately for predicting NDVI variations over the study period (Figure 10).

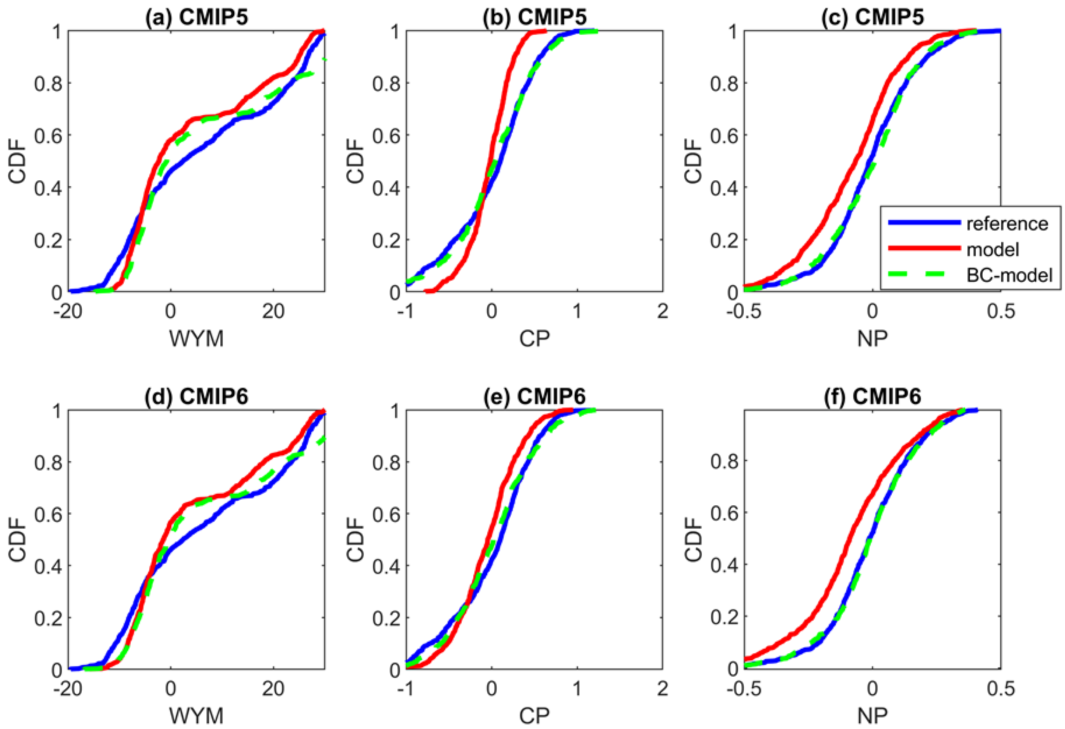

Figure 9. The comparison of the empirical CDFs of referenced (i.e., ERA5 and ERSSTv.5 datasets, here called observation for simplicity), modelled and BC-modelled WYM (a), CP (b) and NP (c) during the historical period from CMIP5. The (d-f) is the same as (a-c) but for the CMIP6.

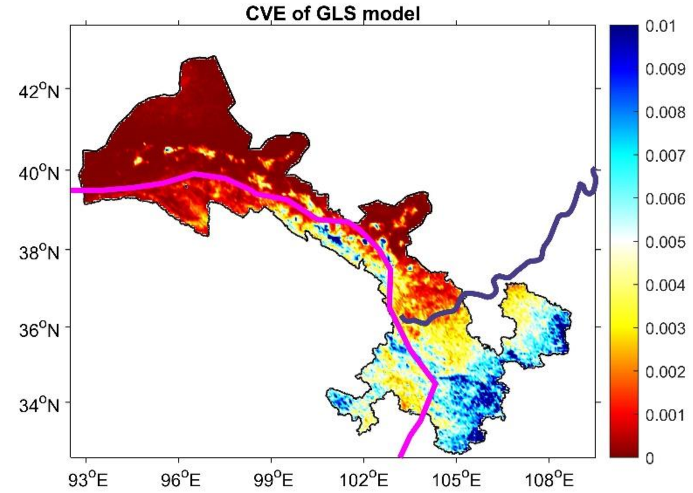

Figure 10. The CVE for the estimated NDVI between February 2000 and January 2020 is based on the GLS models using the LOOCV method. The magenta and purple lines divide the Gansu into three graphically regions (c.f. Figure 1).

4.4.2 NDVI future scenarios

Using cross-validated GLS regression models, the bias-corrected WYM, CP and NP indices are used to project NDVI values for three RCP scenarios (RCP 2.6, RCP 4.5 and RCP 8.5) and three SSP pathways (SSP1-2.6, SSP2-4.5 and SSP5-8.5). For 16 locations (cf. Figure 1), the performances of simulated NDVI over the historical period (from January 2000 to February 2020) are evaluated for 13 CMIP5 (4 models for RCP 2.6) and four CMIP6 climate models using the MSE and the RSD. The MSE values are generally smaller than 0.01 and the RSD values are between 0.77 and 1.1 (close to 1) for all models from CMIP5 and CMIP6, all locations and all scenarios (Figure 11). These results indicate the GLS regression models have an adequate accuracy for reconstructing NDVI variations based on large-scale climate indices.

Figure 12 shows the median changes in the NDVI after 2020, based on 13 CMIP5 (4 models for RCP 2.6) and four CMIP6 models. For CMIP5, in the 2030s, and NDVI values increase for all locations under RCP 2.6 (Figure 12a). NDVI values increase in south locations but decrease in north locations for both the RCP4.5 and RCP 8.5 scenarios (Figure 12c, e). Moreover, under the RCP8.5 scenario, there are fewer locations where NDVI values increase, compared to the RCP4.5 scenario (Figure 12c,e). It suggests that excess greenhouse gas (GHG) emissions may harm the vegetation growth even though the GHG like CO_2 is beneficial for the vegetation growth. Turning to the 2090s, almost all locations of the Gansu region show a decrease in the NDVI for three scenarios (Figure 12b, d, f). For CMIP6, the NDVI values in the 2030s increase compared to the study period (i.e., 2000-2020) for almost locations under three SSPs, and the increase rate is larger over southeast locations (Figure 10g, I, k). In the 2090s, the NDVI values still increase for most locations under SSP1-2.6 (Figure 12h), while NDVI values decrease for almost all locations under SSP2-4.5 (Figure 12j). Under SSP5-8.5,

NDVI values decrease compared to 2030s for north locations but increase for south locations over Gansu (Figure 12l).

Generally, both CMIP5 and CMIP6 show the tendency for vegetation to increase in the near future (2030s). For the long-term future (2090s), except for under SSP1-2.6, CMIP5 and CMIP6 models show decreased tendency of vegetation under most scenarios. The projection results suggest that current climate patterns will promote the vegetation growth over Gansu in the 2030s, but will eventually lead to the overall vegetation reduction in the 2090s. Moreover, the increasing vegetation under SSP1-2.6 suggest that declining emissions can help to alleviate the vegetation reduction in the future.

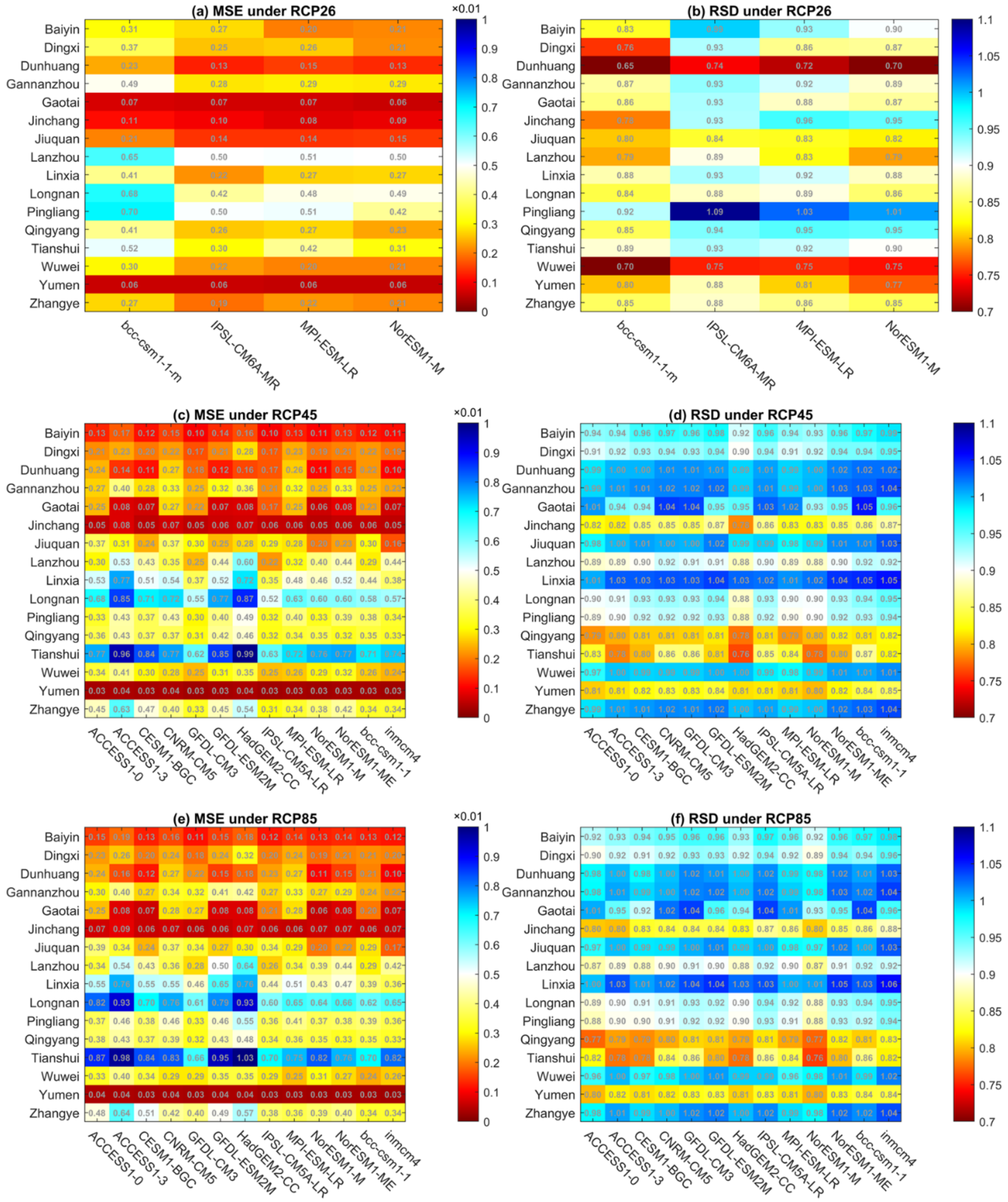
(a) MSE under RCP26
(b) RSD under RCP26
(c) MSE under RCP45
(d) RSD under RCP45
(e) MSE under RCP85
(f) RSD under RCP85
×0.01
Baiyin
Dingxi
Dunhuang
Gannanzhou
Gaotai
Jinchang
Jiuquan
Lanzhou
Linxia
Longnan
Pingliang
Qingyang
Tianshui
Wuwei
Yumen
Zhangye
bcc-csm1-1-m
IPSL-CM6A-MR
MPI-ESM-LR
NorESM1-M
ACCESS1-0
ACCESS1-3
CESM1-BGC
CNRM-CM5
GFDL-CM3
GFDL-ESM2M
HadGEM2-CC
IPSL-CM5A-LR
MPI-ESM-LR
NorESM1-M
NorESM1-ME
bcc-csm1-1
inmcm4

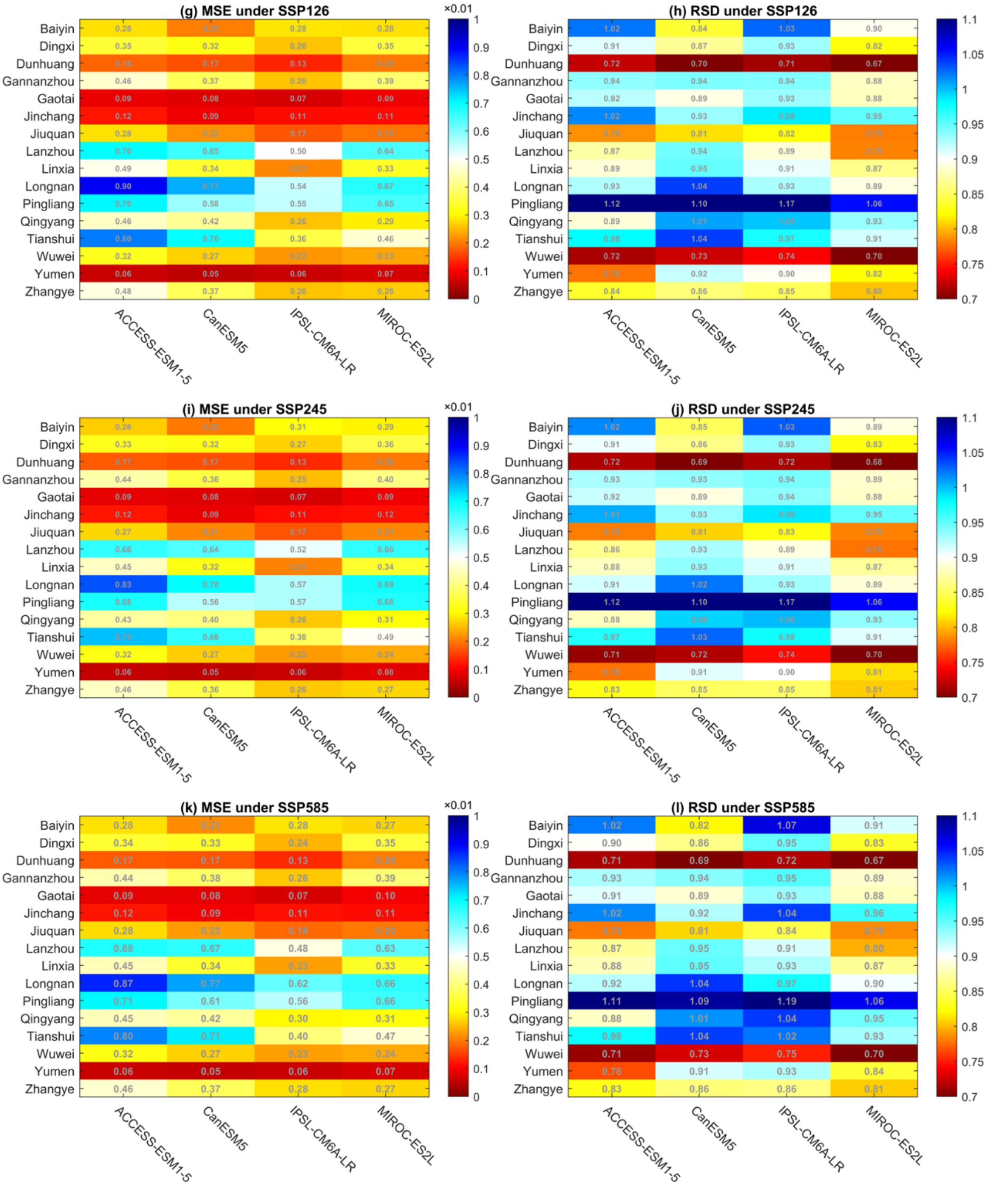

Figure 11. The MSE (a) and RSD (b) between satellite-based and the modelled NDVI from the CMIP5 models under RCP 2.6. The (c-d) and (e-f) are the same as the (a-b) but for RCP 4.5 and RCP 8.5, respectively. The MSE (g) and RSD (h) between satellite-based and the modelled NDVI from the CMIP6 models under SSP1-2.6. The (i-j) and (k-l) are the same as the (g-h) but for SSP2-4.5 and SSP5-8.5, respectively.

466

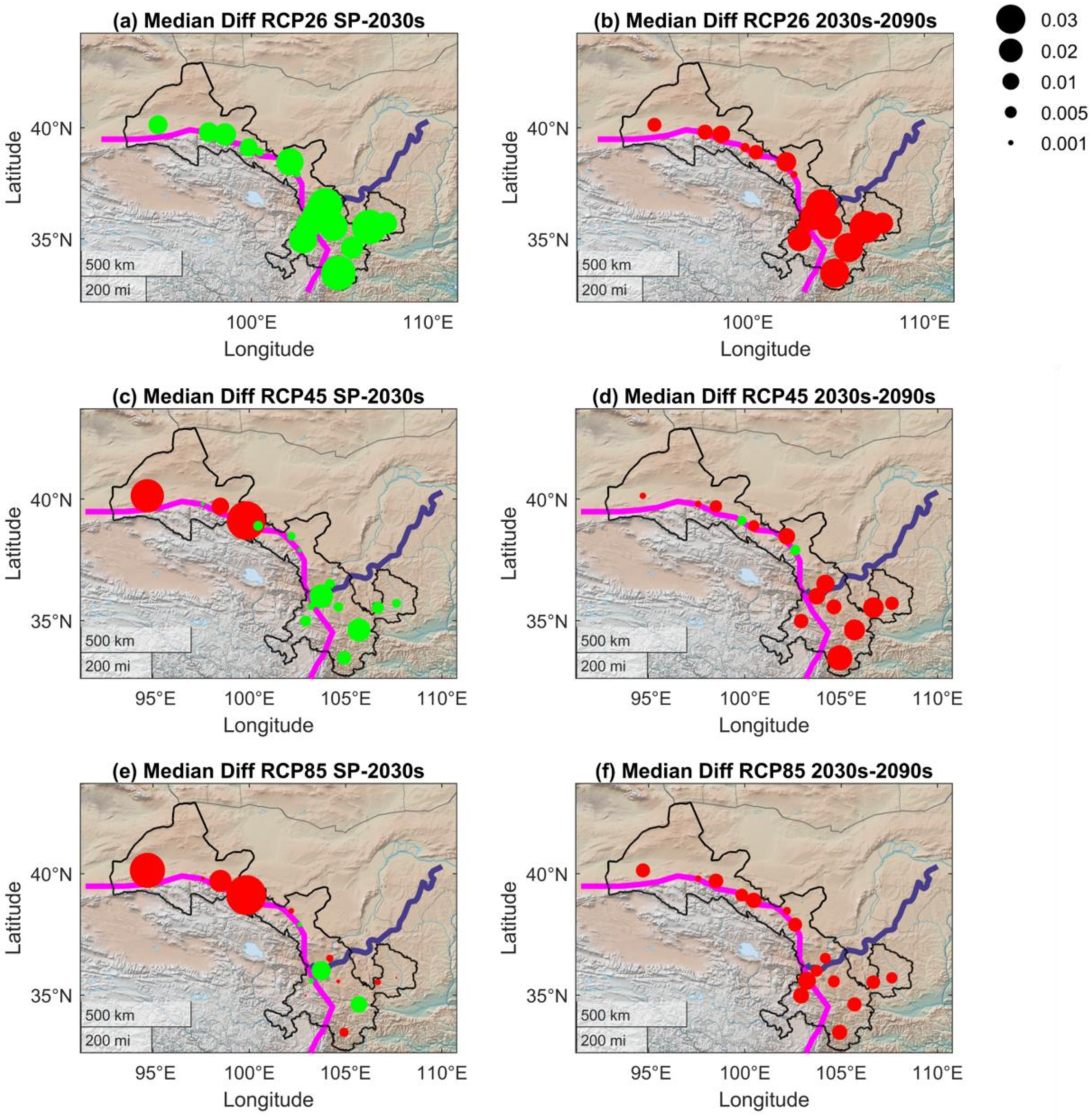
(a) Median Diff RCP26 SP-2030s
(b) Median Diff RCP26 2030s-2090s
(c) Median Diff RCP45 SP-2030s
(d) Median Diff RCP45 2030s-2090s
(e) Median Diff RCP85 SP-2030s
(f) Median Diff RCP85 2030s-2090s
0.03
0.02
0.01
0.005
0.001
Latitude
Longitude
40°N
35°N
95°E
100°E
105°E
110°E
500 km
200 mi

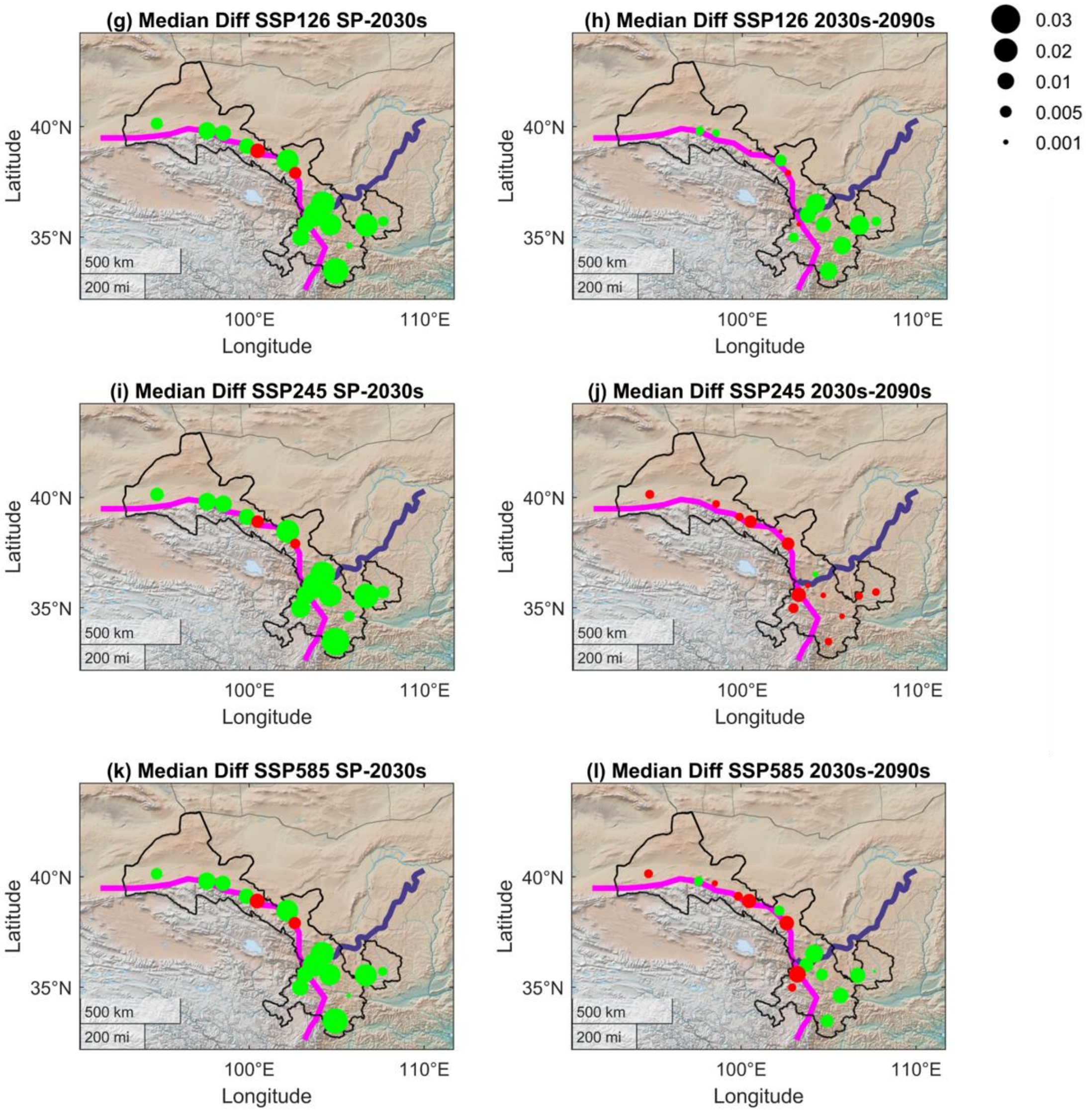

Figure 12. The median NDVI difference between the 2030s and study period (SP), and between 2090s and 2030s across all models from CMIP5 under RCP2.6 (a-b). The (c-d) and (e-f) are the same as the (a-b) but for RCP 4.5 and RCP 8.5, respectively. The median NDVI difference between the 2030s and study period (SP), and between 2090s and 2030s across all models from CMIP6 under SSP1-2.6 (g-h). The (i-j) and (k-l) are the same as the (g-h) but for SSP2-4.5 and SSP5-8.5, respectively. the the The green and red dots represent positive and negative changes, respectively. The magenta and purple lines divide the Gansu into three graphically regions (c.f. Figure 1).

5. Discussion and Conclusion

This study investigates spatiotemporal changes in vegetation cover over the transition zone of Gansu between 2000 and 2020, using a satellite-based NDVI product. Since 2000, Gansu has been increasingly greener, especially in the southern regions. Such vegetation recovery could be explained through the combined impacts of local water and energy dynamics associated with weakening WYM strength, a colder central Pacific Ocean, and a warmer North Pacific Ocean (Figure A5). The local water and energy budgets are controlled by horizontal and vertical dynamics. The vertical thermodynamic (i.e., unchanged CAPE values over the period; Figure A4) is found to have limited impacts on water and energy budgets over the Gansu region (Figure 13). Therefore, the horizontal atmospheric dynamics play a major role in local vegetation variations of Gansu.

As a climate transition region, the water balance in Gansu is controlled by both Asian monsoons and prevailing westerly (Ren et al. 2016). The prevailing westerly brings moisture into North Gansu, which is mainly a water-limited region (Figure 2). Asian monsoons carry moisture into South Gansu, which is mainly an energy-limited region (Figure 2). Then, the mechanisms of large-scale climate variability through horizontal atmospheric dynamics on vegetation are separated into two types: energy-limited regions for South Gansu and water-limited regions for North Gansu (Figure 13).

For energy-limited regions, the weakening WYM, cold phase of CP and warm phase of NP (Figure A5) weaken the monsoon moisture fluxes to inland China, leading to lower precipitation than normal conditions (Figure 13). Less precipitation means less water would be evaporated, thus lower AET in the region (Figure 13). Due to an increasing global temperature trend, the rising local temperature would continue to promote vegetation growths in the energy-limited region, despite locally drying conditions. In the water-limited region, the weakening WYM, cold phase of CP and warm phase of NP (Figure A5) enhance the prevailing westerly through weakening the southwest monsoon moisture fluxes (Figure 13). Westerly and monsoon winds converge in the middle part of Gansu. When the monsoon becomes weaker, prevailing westerly becomes stronger and brings more moisture fluxes to North Gansu (Figure A6). More moisture fluxes over northwest China brought by prevailing westerly are consistent with previous studies (Peng and Zhou 2017; Ren et al. 2016). The warmer temperature and more precipitation promote AET. The increasing water and energy promote vegetation growth in the water-limited region.

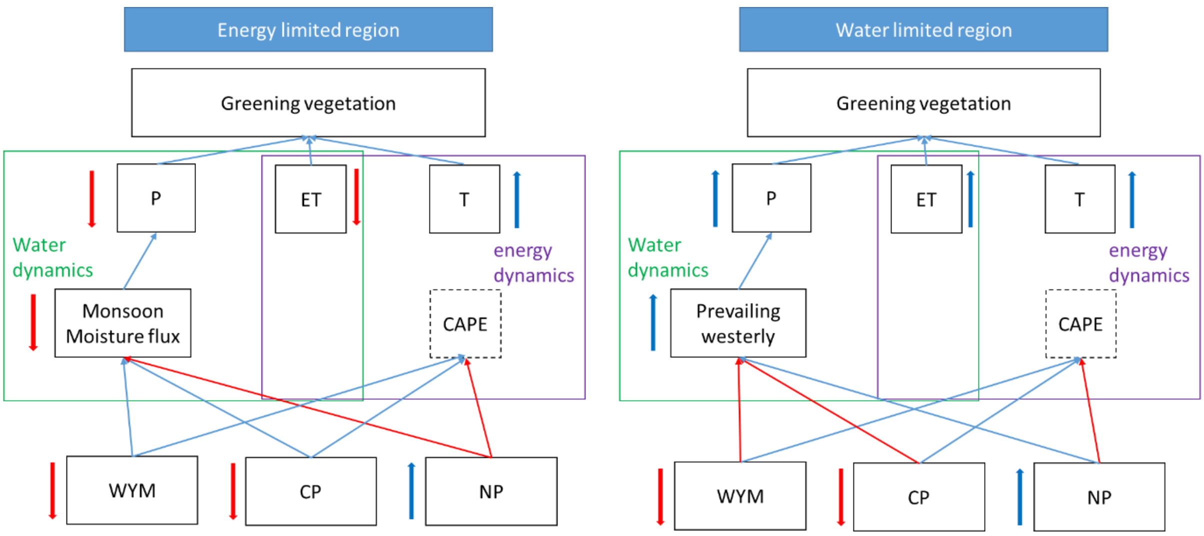

Figure 13. The mechanisms of climate variability effects vegetation. The line arrows represent the linkages between variables, and bold arrows are the trends of variations between February 2000 and January 2020. The blue symbols are for positive or increasing relationships, and the red symbols are for negative or decreasing variations. The dotted box indicates no much changes for the variables (i.e., CAPE).

In addition to climate effects, human activities also affect local vegetation variations. Figure A7 shows possible human effects based on the NDVI residuals, which are the differences between the observed and the GLS modelled NDVI. Both annual variations and residuals of NDVI between 2000 and 2020 can roughly be divided into three stages (Figure A7): Stage 1 is a steady increasing period between 2000 and 2013; Stage 2 is a plateau condition between 2014 and 2016, and Stage 3 is another NDVI increasing period after 2016. The three-stage patterns of the residuals may indicate that the vegetation variations of the 2010s could partly be related to human activities. Gansu is one of the earliest pilot provinces which implement the Grain to Green Program (GTGP) (Li et al. 2015). In the last two decades, Gansu had two rounds of the program. The first round of the GTGP was between 1999 and 2013 and the second round started in 2014 (Gansu Forestry and Grassland Bureau, 2020; available in http://lycy.gansu.gov.cn/contents/79149.html). The increase in the NDVI values during 2000-2013 and after 2016 could thus be partly related to the first and second rounds of GTGP (Li et al., 2015). Between 2014 and 2016, the central government stopped the original GTGP subsidy which may be related to a break in the vegetation increasing trend in Stage 2 of Figure A7.

For future vegetation projection, various studies have used the downscaling methods (Maraun et al. 2010; Sunyer et al. 2015; Thomas et al. 2007). These studies used local climate variables (i.e, precipitation) which are closely related to the topography impacts, and the downscaling processes improved the model results. However, in this study, the NDVI values are estimated based on climate teleconnections, which are not likely to be affected by local topography. Therefore, the downscaling for GCM results will not be included in this manuscript.

Based on the GLS model projections driven by large-scale climate modes of variability derived from CMIP5 and CMIP6 models, the vegetation in Gansu, especially in the southern energy-limited regions will keep increasing in the 2030s, as a response to climate variability and change. However, in the 2090s, Gansu be more likely to experience a decline in vegetation cover based on most of the CMIP5 and CMIP6 projections. The continuous decreases in precipitation will thus lead to a transition from energy-limited regions toward more water-limited regions. Therefore, an increasing desertification risk should be considered for regional development planning and management, and more novel afforestation strategies based on changing monsoons and the Pacific SST conditions needed to be proposed. Overall, this study provides a framework to study possible increasing desertification risk, using climate scenarios from climate models, for the water- and energy- limited transition regions in the world.

Declarations

Funding: This study is supported by the National Natural Science Foundation of China (grant No: 41771262, 41875116). This research is also supported by the Hong Kong Baptist University Faculty Research Grant (No. FRG1/17-18/044 and No. FRG1/16-17/034). This research is conducted using the resources of the High-Performance Cluster Computing Centre, Hong Kong Baptist University, which receives funding from the Research Grant Council, University Grant Committee of the HKSAR and Hong Kong Baptist University. The corresponding author is the awardee of the Accelerator Programme (AP) 2022-24 in the University of the West of England (UWE), Bristol.

Conflicts of interest: The authors have no relevant financial or non-financial interests to disclose.

Availability of data and material:

The NDVI data that support the findings of this study are available in the **National Aeronautics and Space Administration (NASA) Land Processes Distributed Active Archive Center** (LP DAAC; https://e4ftl01.cr.usgs.gov/MOLT/MOD13C2.006/). The climate data that support the findings of this study are openly available in **ERA5-Land monthly averaged data from 1981 to present** at http://doi.org/10.24381/cds.68d2bb30, **ERA5 monthly averaged data on single levels from 1979 to present** at http://doi.org/10.24381/cds.f17050d7, **NOAA Extended Reconstructed Sea Surface Temperature (ERSST), Version 5** at http://doi.org/10.7289/V5T72FNM. The CMIP5 and CMIP6 model data are openly available in the **Earth System Grid Federation** (ESGF; https://esgf-node.llnl.gov/).

Code availability: Not applicable.

Authors' contributions

Qing He: Software, Formal analysis, Validation, Writing - Original Draft, Writing – Review & Editing

Kwok Pan Chun: Conceptualization, Methodology, Investigation, Resources, Data Curation, Writing – Review & Editing, Supervision, Project administration, Funding acquisition

Bastien Dieppois: Writing – Review & Editing

Liang Chen: Writing – Review & Editing, Funding acquisition

Pingyu Fan: Writing – Review & Editing, Data Curation

Emir Toker: Data Curation

Omer Yetemen: Data Curation

Xicai Pan: Writing – Review & Editing, Funding acquisition

References:

An D, Du Y, Berndtsson R, Niu Z, Zhang L, Yuan F (2019) Evidence of climate shift for temperature and precipitation extremes across Gansu Province in China Theoretical and Applied Climatology doi:10.1007/s00704-019-03041-1

Ao J, Sun J (2016) Decadal change in factors affecting winter precipitation over eastern China Climate Dynamics 46:111-121 doi:10.1007/s00382-015-2572-7

Badreldin N, Frankl A, Goossens R (2014) Assessing the spatiotemporal dynamics of vegetation cover as an indicator of desertification in Egypt using multi-temporal MODIS satellite images Arabian Journal of Geosciences 7:4461-4475 doi:10.1007/s12517-013-1142-8

Boé J, Terray L, Habets F, Martin E (2007) Statistical and dynamical downscaling of the Seine basin climate for hydro-meteorological studies International Journal of Climatology 27:1643-1655 doi:10.1002/joc.1602

Cao Y, Zhang W, Wang W (2018) Evaluation of TRMM 3B43 data over the Yangtze River Delta of China Sci Rep 8:5290 doi:10.1038/s41598-018-23603-z

Chen F et al. (2014) Holocene vegetation history, precipitation changes and Indian Summer Monsoon evolution documented from sediments of Xingyun Lake, south-west China Journal of Quaternary Science 29:661-674 doi:10.1002/jqs.2735

Cheng C, Falkenheim V (2016) Gansu. https://www.britannica.com/place/Gansu. Accessed 19 December 2019

Cui L, Shi J (2010) Temporal and spatial response of vegetation NDVI to temperature and precipitation in eastern China Journal of Geographical Sciences 20:163-176 doi:10.1007/s11442-010-0163-4

Dai S, Zhang B, Wang H, Wang Y, Guo L, Wang X, Li D (2011) Vegetation cover change and the driving factors over northwest China 干旱区科学 3:25-33 doi:10.3724/sp.j.1227.2011.00025

Didan K (2015) MOD13C2 MODIS/Terra Vegetation Indices Monthly L3 Global 0.05Deg CMG V006. NASA EOSDIS Land Processes DAAC. doi:https://doi.org/10.5067/MODIS/MOD13C2.006

Dirnböck T, Dullinger S, Grabherr G (2003) A regional impact assessment of climate and land-use change on alpine vegetation Journal of Biogeography 30:401-417 doi:10.1046/j.1365-2699.2003.00839.x

Erasmi S, Propastin P, Kappas M, Panferov O (2009) Spatial Patterns of NDVI Variation over Indonesia and Their Relationship to ENSO Warm Events during the Period 1982–2006 Journal of Climate 22:6612-6623

Eyring V, Bony S, Meehl GA, Senior CA, Stevens B, Stouffer RJ, Taylor KE (2016) Overview of the Coupled Model Intercomparison Project Phase 6 (CMIP6) experimental design and organization Geoscientific Model Development 9:1937-1958 doi:10.5194/gmd-9-1937-2016

Fernandes MR, Aguiar FC, Ferreira MT (2011) Assessing riparian vegetation structure and the influence of land use using landscape metrics and geostatistical tools Landscape and Urban Planning 99:166-177 doi:https://doi.org/10.1016/j.landurbplan.2010.11.001

Ferreira GV, Gong Z, He X, Zhang Y, Andam-Akorful AS (2013) Estimating Total Discharge in the Yangtze River Basin Using Satellite-Based Observations Remote Sensing 5 doi:10.3390/rs5073415

Fowler HJ, Blenkinsop S, Tebaldi C (2007) Linking climate change modelling to impacts studies: recent advances in downscaling techniques for hydrological modelling International Journal of Climatology 27:1547-1578 doi:10.1002/joc.1556

Gao T, Luo M, Lau N-C, Chan TO (2020) Spatially Distinct Effects of Two El Niño Types on Summer Heat Extremes in China Geophysical Research Letters 47:e2020GL086982 doi:10.1029/2020GL086982

Gokmen M, Vekerdy Z, Verhoef W, Batelaan O (2013) Satellite-based analysis of recent trends in the ecohydrology of a semi-arid region Hydrol Earth Syst Sci 17:3779-3794 doi:10.5194/hess-17-3779-2013

Grillakis MG, Koutroulis AG, Tsanis IK (2013) Multisegment statistical bias correction of daily GCM precipitation output Journal of Geophysical Research: Atmospheres 118:3150-3162 doi:10.1002/jgrd.50323

Hamed KH (2008) Trend detection in hydrologic data: The Mann–Kendall trend test under the scaling hypothesis Journal of Hydrology 349:350-363 doi:https://doi.org/10.1016/j.jhydrol.2007.11.009

Hamed KH, Ramachandra Rao A (1998) A modified Mann-Kendall trend test for autocorrelated data Journal of Hydrology 204:182-196 doi:https://doi.org/10.1016/S0022-1694(97)00125-X

Han L, Zhang Z, Zhang Q, Wan X (2015) Desertification assessments in the Hexi corridor of northern China's Gansu Province by remote sensing Natural Hazards 75:2715-2731 doi:10.1007/s11069-014-1457-0

He Q, Chun KP, Sum Fok H, Chen Q, Dieppois B, Massei N (2020) Water storage redistribution over East China, between 2003 and 2015, driven by intra- and inter-annual climate variability Journal of Hydrology 583:124475 doi:https://doi.org/10.1016/j.jhydrol.2019.124475

Hersbach H et al. (2019) ERA5 monthly averaged data on single levels from 1979 to present. Copernicus Climate Change Service (C3S) Climate Data Store (CDS). doi:10.24381/cds.f17050d7

Hou J, Du L, Liu K, Hu Y, Zhu Y (2019) Characteristics of vegetation activity and its responses to climate change in desert/grassland biome transition zones in the last 30 years based on GIMMS3g Theoretical and Applied Climatology 136:915-928 doi:10.1007/s00704-018-2527-0

Huang B et al. (2017) Extended reconstructed sea surface temperature, version 5 (ERSSTv5): upgrades, validations, and intercomparisons Journal of Climate 30:8179-8205

Javadian M, Behrangi A, Smith WK, Fisher JB (2020) Global Trends in Evapotranspiration Dominated by Increases across Large Cropland Regions Remote Sensing 12 doi:10.3390/rs12071221

Jiang G et al. (2011) Effects of ENSO-linked climate and vegetation on population dynamics of sympatric rodent species in semiarid grasslands of Inner Mongolia, China Canadian Journal of Zoology 89:678-691 doi:10.1139/z11-048

Jiang W et al. (2006) Reconstruction of climate and vegetation changes of Lake Bayanchagan (Inner Mongolia): Holocene variability of the East Asian monsoon Quaternary Research 65:411-420 doi:https://doi.org/10.1016/j.yqres.2005.10.007

Jiang W et al. (2017) Reconstruction of climate and vegetation changes of Lake Bayanchagan (Inner Mongolia): Holocene variability of the East Asian monsoon Quaternary Research 65:411-420 doi:10.1016/j.yqres.2005.10.007

Kendall MG (1975) Rank correlation methods. Rank correlation methods. Griffin, Oxford, England

Khaliq MN, Ouarda TBMJ, Gachon P (2009) Identification of temporal trends in annual and seasonal low flows occurring in Canadian rivers: The effect of short- and long-term persistence Journal of Hydrology 369:183-197 doi:https://doi.org/10.1016/j.jhydrol.2009.02.045

Krull ES et al. (2005) Recent vegetation changes in central Queensland, Australia: Evidence from δ13C and 14C analyses of soil organic matter Geoderma 126:241-259 doi:https://doi.org/10.1016/j.geoderma.2004.09.012

Lee E, Chase TN, Rajagopalan B, Barry RG, Biggs TW, Lawrence PJ (2009) Effects of irrigation and vegetation activity on early Indian summer monsoon variability International Journal of Climatology 29:573-581 doi:10.1002/joc.1721

Li C, Li G (2000) The NPO/ NAO and interdecadal climate variation in China Advances in Atmospheric Sciences 17:555-561 doi:10.1007/s00376-000-0018-5

Li H, Sheffield J, Wood EF (2010a) Bias correction of monthly precipitation and temperature fields from Intergovernmental Panel on Climate Change AR4 models using equidistant quantile matching Journal of Geophysical Research: Atmospheres 115 doi:10.1029/2009JD012882

Li K, Liu X, Wang Y, Herzschuh U, Ni J, Liao M, Xiao X (2017) Late Holocene vegetation and climate change on the southeastern Tibetan Plateau: Implications for the Indian Summer Monsoon and links to the Indian Ocean Dipole Quaternary Science Reviews 177:235-245 doi:https://doi.org/10.1016/j.quascirev.2017.10.020

Li S, Yan J, Liu X, Wan J (2013) Response of vegetation restoration to climate change and human activities in Shaanxi-Gansu-Ningxia Region Journal of Geographical Sciences 23:98-112 doi:10.1007/s11442-013-0996-8

Li S, Yang S, Liu X, Liu Y, Shi M (2015) NDVI-Based Analysis on the Influence of Climate Change and Human Activities on Vegetation Restoration in the Shaanxi-Gansu-Ningxia Region, Central China Remote Sensing 7:11163-11182

Li X, Shi Q, Guo J (2009) The response of NDVI to climate variability in Northwest Arid Area of China from 1981 to 2001 Journal of Arid Land Resources and Environment 23:12-16

Li Z, Li X, Wei D, Xu X, Wang H (2010b) An assessment of correlation on MODIS-NDVI and EVI with natural vegetation coverage in Northern Hebei Province, China Procedia Environmental Sciences 2:964-969 doi:https://doi.org/10.1016/j.proenv.2010.10.108

Los SO (2013) Analysis of trends in fused AVHRR and MODIS NDVI data for 1982–2006: Indication for a CO2 fertilization effect in global vegetation Global Biogeochemical Cycles 27:318-330 doi:10.1002/gbc.20027

Lü A, Zhu W, Jia S (2012) Assessment of the sensitivity of vegetation to El-Niño/Southern Oscillation events over China Advances in Space Research 50:1362-1373 doi:https://doi.org/10.1016/j.asr.2012.06.033

Lv A, Qu B, Jia S, Zhu W (2019) Influence of three phases of El Niño–Southern Oscillation on daily precipitation regimes in China Hydrol Earth Syst Sci 23:883-896 doi:10.5194/hess-23-883-2019

Mann HB (1945) Nonparametric Tests Against Trend Econometrica 13:245-259 doi:10.2307/1907187

Mao J et al. (2016) Human-induced greening of the northern extratropical land surface Nature Climate Change 6:959-963 doi:10.1038/nclimate3056

Maraun D et al. (2010) Precipitation downscaling under climate change: Recent developments to bridge the gap between dynamical models and the end user Reviews of Geophysics 48 doi:https://doi.org/10.1029/2009RG000314

Miao C, Su L, Sun Q, Duan Q (2016) A nonstationary bias-correction technique to remove bias in GCM simulations Journal of Geophysical Research: Atmospheres 121:5718-5735 doi:10.1002/2015JD024159

Mkhabela MS, Bullock P, Raj S, Wang S, Yang Y (2011) Crop yield forecasting on the Canadian Prairies using MODIS NDVI data Agricultural and Forest Meteorology 151:385-393 doi:https://doi.org/10.1016/j.agrformet.2010.11.012

Mohammat A et al. (2013) Drought and spring cooling induced recent decrease in vegetation growth in Inner Asia Agricultural and Forest Meteorology 178-179:21-30 doi:https://doi.org/10.1016/j.agrformet.2012.09.014

Muñoz S, J. (2019) C3S ERA5-Land reanalysis. Copernicus Climate Change Service (C3S) Climate Data Store (CDS). doi:10.24381/cds.68d2bb30

Ouyang R, Liu W, Fu G, Liu C, Hu L, Wang H (2014) Linkages between ENSO/PDO signals and precipitation, streamflow in China during the last 100 years Hydrology and Earth System Sciences 18:3651-3661 doi:10.5194/hess-18-3651-2014

Panofsky HA, Brier GW (1958) Some applications of statistics to meteorology. Mineral Industries Extension Services, College of Mineral Industries …,

Parsons AJ, Abrahams AD (1994) Geomorphology of Desert Environments. In: Abrahams AD, Parsons AJ (eds) Geomorphology of Desert Environments. Springer Netherlands, Dordrecht, pp 3-12. doi:10.1007/978-94-015-8254-4_1

Peng D, Zhou T (2017) Why was the arid and semiarid northwest China getting wetter in the recent decades? Journal of Geophysical Research: Atmospheres 122:9060-9075 doi:https://doi.org/10.1002/2016JD026424

Piao S, Wang X, Ciais P, Zhu B, Wang TAO, Liu JIE (2011) Changes in satellite-derived vegetation growth trend in temperate and boreal Eurasia from 1982 to 2006 Global Change Biology 17:3228-3239 doi:10.1111/j.1365-2486.2011.02419.x

Ren G, Yuan Y, Liu Y, 任玉玉 Y, Wang T (2016) Change in precipitation over Northwest China Arid Zone Research 33:1-19

Schimel D et al. (2000) Contribution of Increasing CO₂ and Climate to Carbon Storage by Ecosystems in the United States Science 287:2004 doi:10.1126/science.287.5460.2004

Sen PK (1968) Estimates of the Regression Coefficient Based on Kendall's Tau Journal of the American Statistical Association 63:1379-1389 doi:10.1080/01621459.1968.10480934

Shukla KA, Ojha SC, Singh PR, Pal L, Fu D (2019) Evaluation of TRMM Precipitation Dataset over Himalayan Catchment: The Upper Ganga Basin, India Water 11 doi:10.3390/w11030613

Sunyer MA et al. (2015) Inter-comparison of statistical downscaling methods for projection of extreme precipitation in Europe Hydrol Earth Syst Sci 19:1827-1847 doi:10.5194/hess-19-1827-2015

Swain S, Hayhoe K (2015) CMIP5 projected changes in spring and summer drought and wet conditions over North America Climate Dynamics 44:2737-2750 doi:10.1007/s00382-014-2255-9

Tasser E, Tappeiner U (2002) Impact of land use changes on mountain vegetation Applied Vegetation Science 5:173-184 doi:10.1111/j.1654-109X.2002.tb00547.x

Taylor KE, Stouffer RJ, Meehl GA (2012) An Overview of CMIP5 and the Experiment Design Bulletin of the American Meteorological Society 93:485-498 doi:10.1175/bams-d-11-00094.1

Thomas C, Nicholas LB, David F-M (2007) GCM grid-box choice and predictor selection associated with statistical downscaling of daily precipitation over Northern Ireland Climate Research 34:145-160

Tong S, Li X, Zhang J, Bao Y, Bao Y, Na L, Si A (2019) Spatial and temporal variability in extreme temperature and precipitation events in Inner Mongolia (China) during 1960–2017 Science of The Total Environment 649:75-89 doi:https://doi.org/10.1016/j.scitotenv.2018.08.262

Trenberth KE, Fasullo JT, Mackaro J (2011) Atmospheric Moisture Transports from Ocean to Land and Global Energy Flows in Reanalyses Journal of Climate 24:4907-4924 doi:10.1175/2011JCLI4171.1

Turkington T, Timbal B, Rahmat R (2019) The impact of global warming on sea surface temperature based El Niño–Southern Oscillation monitoring indices International Journal of Climatology 39:1092-1103 doi:10.1002/joc.5864

Wang G, Ding Y, Shen Y, Lai Y (2003) Environmental degradation in the Hexi Corridor region of China over the last 50 years and comprehensive mitigation and rehabilitation strategies Environmental Geology 44:68-77 doi:10.1007/s00254-002-0736-3

Wang L, Chen W, Huang G, Zeng G (2017a) Changes of the transitional climate zone in East Asia: past and future Climate Dynamics 49:1463-1477 doi:10.1007/s00382-016-3400-4

Wang L, Chen W, Zhou W (2014a) Assessment of future drought in Southwest China based on CMIP5 multimodel projections Advances in Atmospheric Sciences 31:1035-1050 doi:10.1007/s00376-014-3223-3

Wang N, Jiang J, Chen M, Bai S (2018) Spatio-temporal Variation of NDVI and Its Response to Regional Climate in Gansu Province Forest Resources Management 000:109-116

Wang P, Xie D, Zhou Y, E Y, Zhu Q (2014b) Estimation of net primary productivity using a process-based model in Gansu Province, Northwest China Environmental Earth Sciences 71:647-658 doi:10.1007/s12665-013-2462-4

Wang X, Wang T, Liu D, Guo H, Huang H, Zhao Y (2017b) Moisture-induced greening of the South Asia over the past three decades Global Change Biology 23:4995-5005 doi:10.1111/gcb.13762

Webster PJ, Yang S (1992) Monsoon and Enso: Selectively Interactive Systems Quarterly Journal of the Royal Meteorological Society 118:877-926 doi:10.1002/qj.49711850705

Weng H, Wu G, Liu Y, Behera SK, Yamagata T (2011) Anomalous summer climate in China influenced by the tropical Indo-Pacific Oceans Climate Dynamics 36:769-782 doi:10.1007/s00382-009-0658-9

Xia H et al. (2019) Forest Phenology Dynamics to Climate Change and Topography in a Geographic and Climate Transition Zone: The Qinling Mountains in Central China Forests 10 doi:10.3390/f10111007

Xiao M, Zhang Q, Singh VP (2015) Influences of ENSO, NAO, IOD and PDO on seasonal precipitation regimes in the Yangtze River basin, China International Journal of Climatology 35:3556-3567 doi:10.1002/joc.4228

Xu Y, Yang J, Chen Y (2016) NDVI-based vegetation responses to climate change in an arid area of China Theoretical and Applied Climatology 126:213-222 doi:10.1007/s00704-015-1572-1

Yang J et al. (2019) Changing Trends of NDVI and Their Responses to Climatic Variation in Different Types of Grassland in Inner Mongolia from 1982 to 2011 Sustainability 11 doi:10.3390/su11123256

Yang L, Sun G, Zhi L, Zhao J (2018) Negative soil moisture-precipitation feedback in dry and wet regions Scientific Reports 8:4026 doi:10.1038/s41598-018-22394-7

Yang Y, Donohue RJ, McVicar TR, Roderick ML, Beck HE (2016) Long-term CO2 fertilization increases vegetation productivity and has little effect on hydrological partitioning in tropical rainforests Journal of Geophysical Research: Biogeosciences 121:2125-2140 doi:10.1002/2016JG003475

Zhang J, Dong W, Fu C, Wu L (2003) The influence of vegetation cover on summer precipitation in China: A statistical analysis of NDVI and climate data Advances in Atmospheric Sciences 20:1002 doi:10.1007/BF02915523

Zhao Q, Zhu Z, Zeng H, Zhao W, Myneni RB (2020) Future greening of the Earth may not be as large as previously predicted Agricultural and Forest Meteorology 292-293:108111 doi:https://doi.org/10.1016/j.agrformet.2020.108111

Zhao S (1983) A NEW SCHEME FOR COMPREHENSIVE PHYSICAL REGIONALIZATION IN CHINA Acta Geographica Sinica 50:1-10 doi:10.11821/xb198301001

Zhao X, Tan K, Fang J (2011) NDVI-based interannual and seasonal variations of vegetation activity in Xinjiang during the period of 1982–2006 Arid Zone Research 28:10-16

Zhao Y, Yu Z (2012) Vegetation response to Holocene climate change in East Asian monsoon-margin region Earth-Science Reviews 113:1-10 doi:https://doi.org/10.1016/j.earscirev.2012.03.001

Zhou B, Xia D (2012) Interdecadal change of the connection between winter North Pacific Oscillation and summer precipitation in the Huaihe River valley Science China Earth Sciences 55:2049-2057 doi:10.1007/s11430-012-4499-8

Zhou Z, Ding Y, Shi H, Cai H, Fu Q, Liu S, Li T (2020) Analysis and prediction of vegetation dynamic changes in China: Past, present and future Ecological Indicators 117:106642 doi:https://doi.org/10.1016/j.ecolind.2020.106642

Appendix

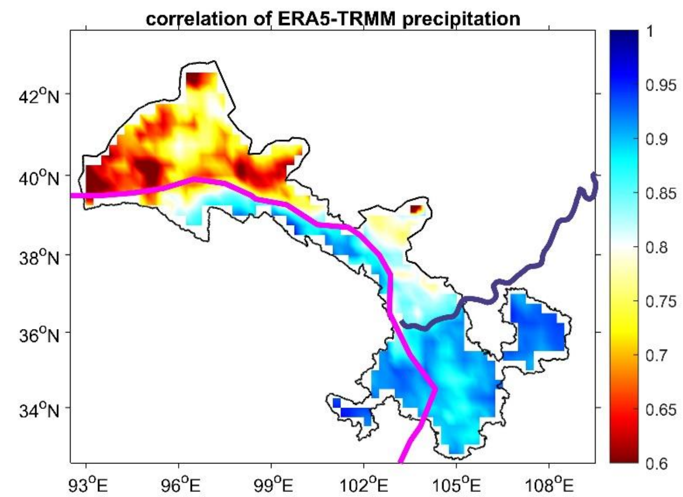

Figure A1. The correlation between ERA5 and TRMM derived precipitation at significance level of $p < 0.05$.

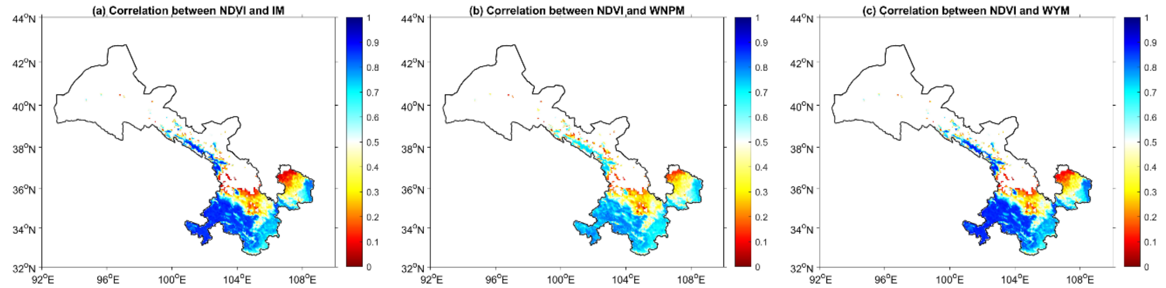

Figure A2. The correlation between NDVI and Asian monsoons, including IM (a), WNPM (b) and WYM (c).

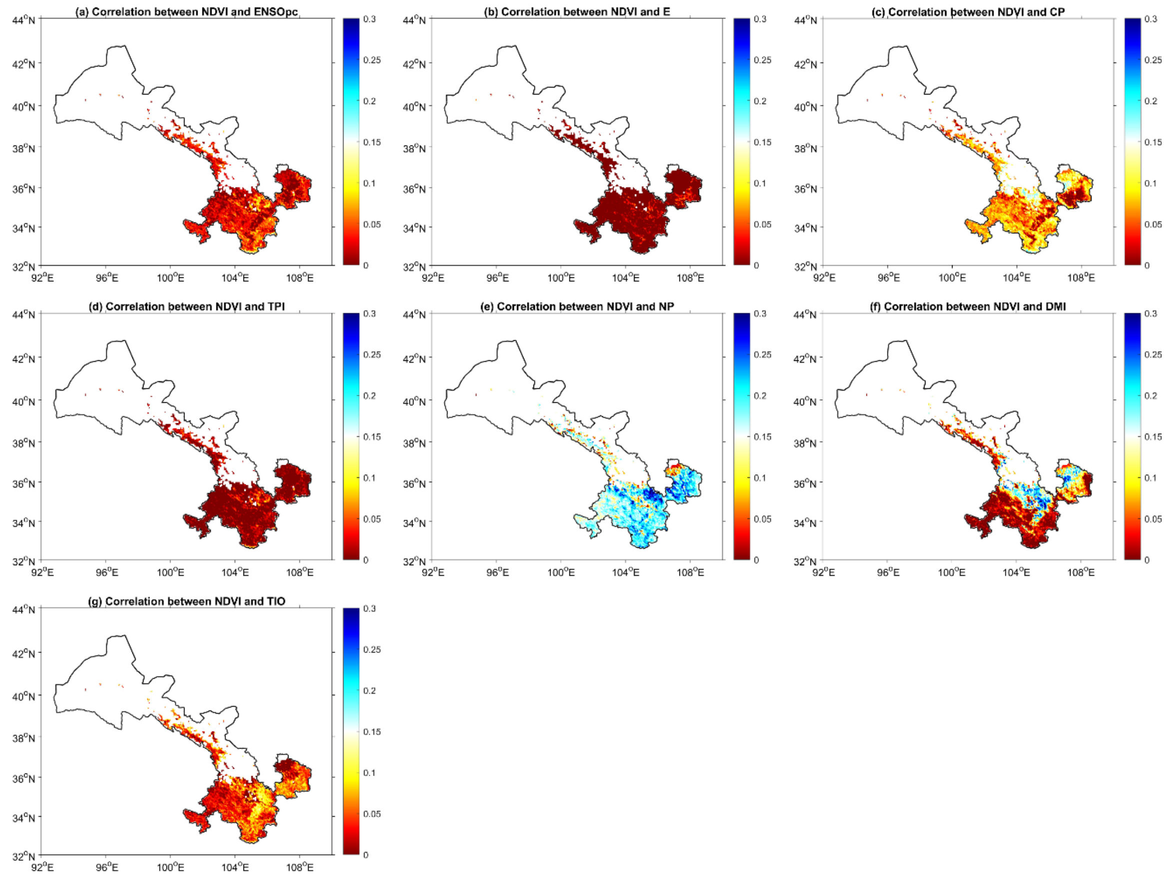

Figure A3. The correlation between NDVI and SST indices in Pacific (a-e) and Indian Ocean (f-g).

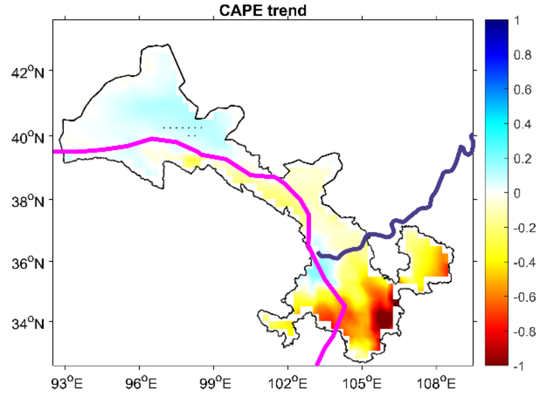

Figure A4. The CAPE trend map between February 2000 and 2020 January. Black dots indicate significant values at 0.1 significance level according to the MK-test.

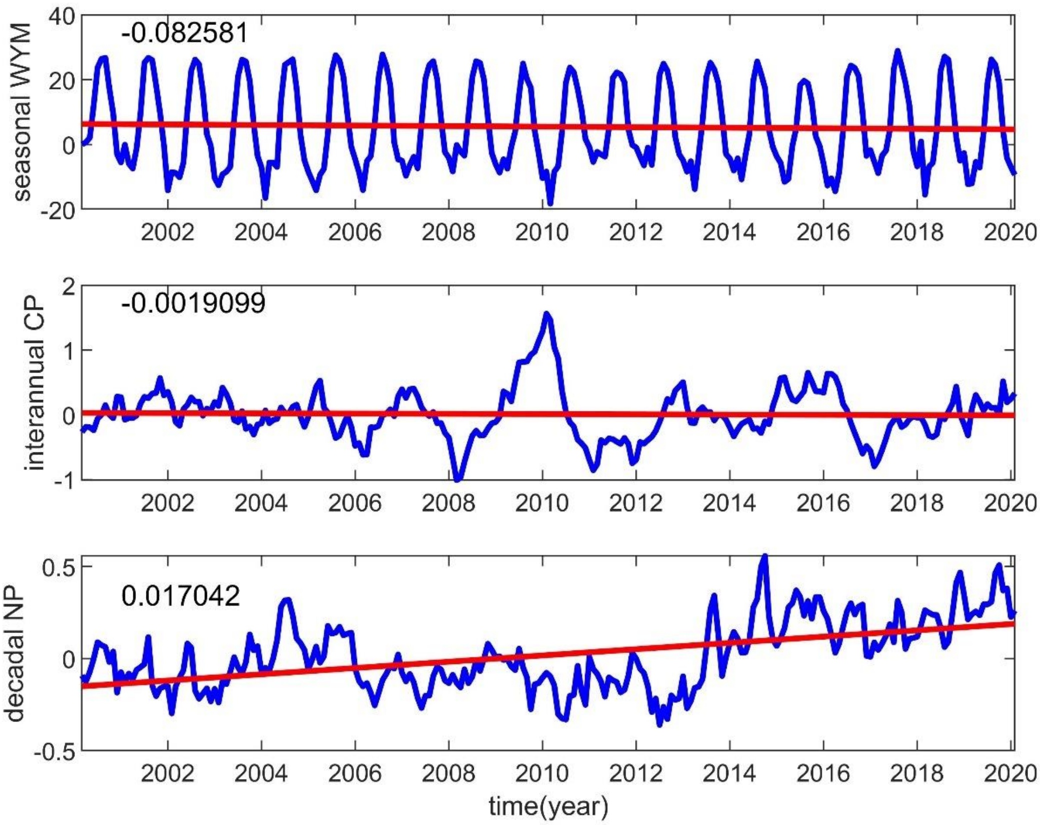

Figure A5. The time series (blue) with trend line (red) of WYM, CP and NP.

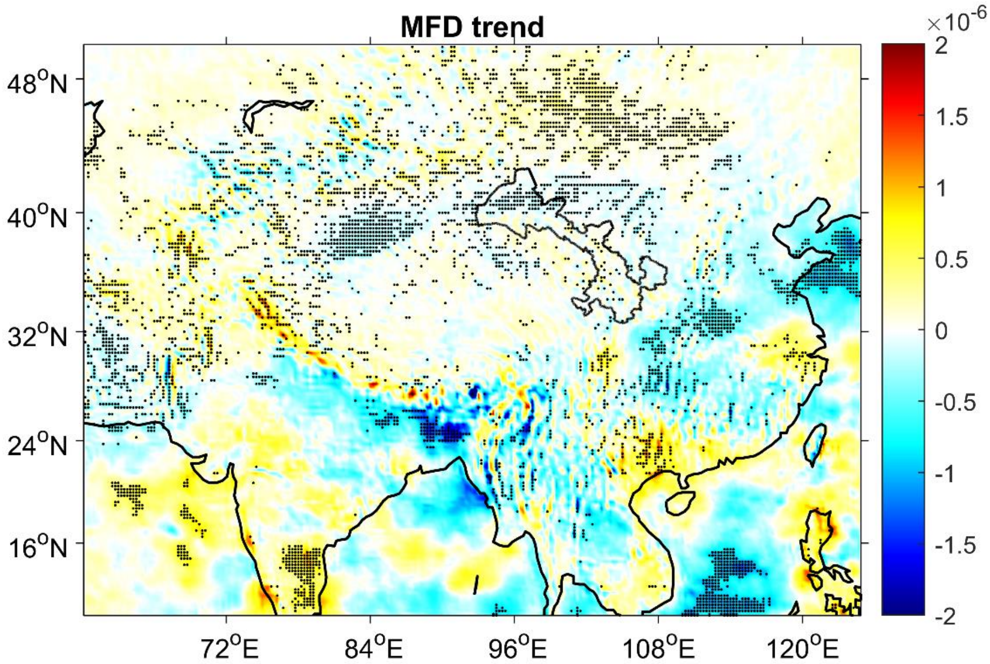

Figure A6. The trend of vertical integrated moisture flux divergence during February 2000 and January 2020. Black dots indicate significant values at 0.1 significance level.

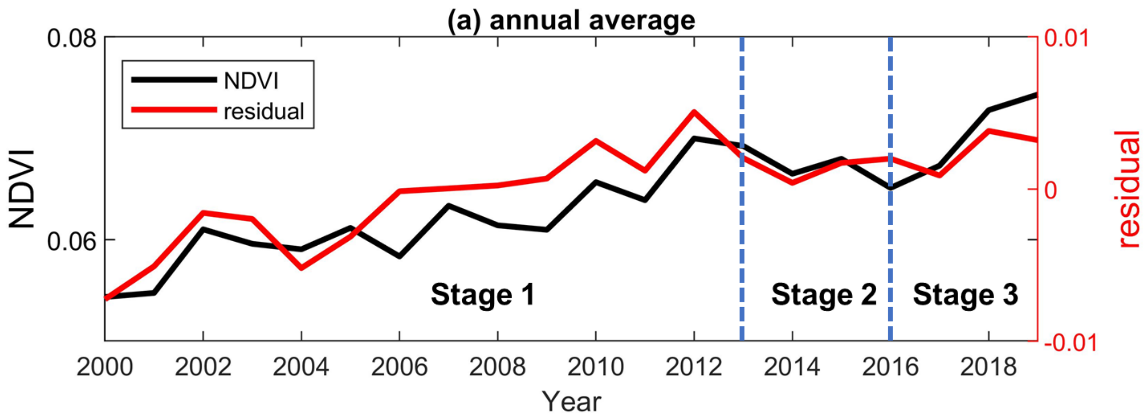

Figure A7. The annual averaged of NDVI and residual NDVI over the whole Gansu during 2000 and 2019.